Experiments on the Morphological Controls of Velocity Inversions in Bedrock Canyons

by

Brendan Hunt

B.Sc., Environmental Geography, University of Guelph, 2007

Thesis Submitted in Partial Fulfillment of the
Requirements for the Degree of
Master of Science

in the
Department of Geography
Faculty of Environment

SIMON FRASER UNIVERSITY
Spring 2017

Approval

Name:	**Brendan Hunt**
Degree:	**Master of Science**
Title:	**Experiments on the Morphological Controls of Velocity Inversions in Bedrock Canyons**
Examining Committee:	**Chair: Nadine Schuurman** Professor **Jeremy Venditti** Senior Supervisor Professor **Michael Church** Supervisor Professor Emeritus Department of Geography University of British Columbia **John Clague** Supervisor Professor Department of Earth Sciences **Jason Leach** External Examiner Assistant Professor
Date Defended/Approved:	April 3, 2017

Abstract

A recent investigation of flow through bedrock canyons of the Fraser River revealed that plunging flows occur where the canyons are laterally constrained and have low width-to-depth ratios. An experimental investigation was undertaken to reproduce the plunging flow fields observed in the Fraser canyons and to explore the influence of morphological controls on the occurrence and relative strength of plunging flow in bedrock canyons. Observations show that the plunging flow structure can be produced by accelerating the flow at the canyon entrance either over submerged sills or through lateral constrictions at the top of a scour pool entrance slope. The occurrence and strength of plunging flow into a scour pool can be enhanced by sill height, amount of lateral constriction, pool entrance slope, discharge, and reduced width-to-depth ratio. Plunging flow greatly enhances the potential for incision to occur along the channel bed and is an extreme departure from the assumptions of steady, uniform flow in bedrock incision models, highlighting the need for improved formulations that account for fluid flow.

Keywords: plunging flow; Type B flow; bedrock canyons; channel morphology; channel constriction

Table of Contents

List of Tables

List of Figures

Introduction

Bedrock rivers play an important role in erosional landscape evolution. A better understanding of bedrock incision mechanisms and processes is essential to the study of this linkage (Whipple et al., 2013). There has been a substantial effort to advance our understanding of landscape evolution using numerical models that link the interactions among channel incision, topography, tectonics, and climate (Kirkby, 1986; Willgoose et al., 1991; Howard, 1994; Tucker and Slingerland, 1994, 1997; Braun and Sambridge, 1997; Tucker and Bras, 1998; Willett, 1999; Tucker et al., 2001a, 2001b; Coulthard et al., 2002). These models integrate our understanding of bedrock channel incision with other geomorphic processes to predict the evolution of landscapes over geologic time scales. The flow and bedrock erosion processes in channels are parameterized in these landscape evolution models using the stream power model (Howard and Kerby, 1983) that assumes incision rates are some function of flow, parameterized as a function of the contributing basin area, which controls discharge and channel slope. These models do not incorporate any details of the hydraulics or specific erosion processes. Our understanding of flow and bedrock erosion processes is presently improving and we are approaching a stage where directly coupled models of flow, sediment transport processes and incision may be possible.

The principal processes of bedrock erosion are abrasion by bedload and suspended load and plucking of bedrock blocks, which can be initially fractured by impacting sediments (Chatanantavet and Parker, 2009). Weathering processes precondition the rock to these processes (Murphy et al., 2016). Several incision models have been developed to quantify and predict bedrock incision rates by these processes, including the 1) saltation-abrasion model (Sklar and Dietrich, 2004), 2) total load erosion model (Lamb et al., 2008), 3) abrasion, plucking, and macro-abrasion model (Chatanantavet and Parker, 2009), and 4) plucking model (Lamb et al., 2015; Larsen and Lamb, 2016). The saltation-abrasion model predicts vertical incision rates by saltating bedload particle collisions on bare bedrock surfaces. The model necessarily incorporates a tools and cover effect produced by variable sediment supply, where the efficiency of bedrock erosion is buffered by the surface area protected from impacting sediment. The total load erosion model builds upon the saltation-abrasion model and accounts for not only bedload abrasion by saltation, but also abrasion by suspended load. The model corrects an inherent problem with the saltation-abrasion model in which erosion ceases when particles begin to be intermittently suspended (Scheingross et al., 2014). The abrasion, plucking, and

macroabrasion model improves upon prior bedrock incision models by incorporating the erosional mechanisms of plucking, abrasion by saltating bedload, and macroabrasion, which serves to break rock into pluckable sizes and is mediated by particle impacts. The plucking model predicts erosion rates based on the threshold for blocks to slide out of position based on their protrusion into the flow, hydraulic lift forces, and the friction angle of the block (Lamb et al., 2015; Larsen and Lamb, 2016).

The current generation of models assumes that incision rate scales with stream power (Howard and Kerby, 1983) or boundary shear stress and assumes steady, uniform flow conditions. In mechanistic incision models, simplifications of the reach-scale fluid stresses acting along the channel boundary are made using either the depth-slope product (Chatanantavet and Parker, 2009; Sklar and Dietrich, 2004) or the law of the wall (Lamb et al., 2008). However, some recent work has used ray-isovel models (Wobus et al., 2008; DiBiase and Whipple, 2011; Nelson and Seminara, 2011) developed by Houjou et al. (1990) and Kean and Smith (2004), which provide a more reasonable method of distributing shear stress across the channel cross-section. Recently, the saltation abrasion (Lai et al., 2011) and plucking models (Larsen and Lamb, 2016) have been coupled with a 2D hydrodynamic model. While these efforts are certainly improvements on the steady uniform flow approximations commonly used with incision models, none of these models has been tested against observations of flow patterns in bedrock rivers and that limits our ability to accurately quantify incision rates and simulate landscape evolution.

Using an acoustic Doppler profiler, Venditti et al. (2014) provided the first three-dimensional observations of the flow structure in bedrock canyons. In canyons that are laterally constrained and had low width-to-depth ratios, they observed a velocity inversion where a high-velocity core developed at the canyon entrance, plunged below the water surface, followed the channel bed down into a scour pool, and ultimately dissipated downstream. The high-velocity core re-appeared with each narrowing of the canyons. Venditti et al. (2014) showed that the downward-directed high-velocity core was compensated by upwelling of highly turbulent, low-velocity fluid along the canyon walls in the form of intermittent coherent flow structures that formed boils at the water surface. They hypothesized that this upwelling reduces near-bed dynamic pressure and draws the higher-velocity flow entering the canyons to advect along the bed, creating a positive feedback in which the high-velocity fluid near the bed contributes to intense upwelling along the walls. Venditti et al. (2014) suggested that the initiation of the plunging flow structure is caused by the acceleration of flow through a lateral constriction,

forcing a canyon to deepen until reaching morphodynamic equilibrium with the near-bed flow and the sediment transport responsible for incision. This suggestion is consistent with the views of several researchers (Attal et al., 1998; Hancock et al., 1998; Finnegan et al., 2005), who suggested that enhancement of erosion along the bed occurs where channels narrow and become steeper, with an accompanying increase in flow velocities relative to upstream and downstream flow.

The observations of Venditti et al. (2014) suggest that steady, uniform flow conditions do not adequately represent the flow in bedrock canyons. The plunging high-velocity core observed in bedrock canyons enhances boundary shear stresses by drawing high-velocity fluid and sediment toward the bed. A more complete representation of the flow processes operating along channel boundaries is required for more realistic application of bedrock incision models. At the scale of landscape evolution, a suitable generalization of flow processes must be adopted; however, this generalization must be consistent with our observations at the process scale.

Phenomena of plunging flow similar to that described by Venditti et al. (2014) have been described in the classical hydraulics literature (Escande, 1939; Kindsvater, 1964; Borland-Coogan, 1980; Fritz and Hager, 1998; Kabiri-Samani et al., 2010). Escande (1939) characterized a plunging flow regime where the main flow is directed along the downstream slope of a weir with a surface roller vortex and upstream flow over the slope (Fritz and Hager, 1998). This phenomenon has been termed “plunging flow”, “plunging jet”, or “impinging jet” by several authors for its relevance to flow over weirs (Escande, 1939; Wu and Rajaratnam, 1996; Fritz and Hager, 1998; Kabiri-Samani et al., 2010), or as “plunging jump” or “drowning machine” for its relevance to public safety at low-head dams (Borland-Coogan, 1980; Tschantz and Wright, 2011). Surprisingly little, however, is known about the geometric constraints responsible for initiating this plunging flow regime. Analogues may also be drawn to velocity inversions in alluvial pools in which efforts have been made to test the flow reversal hypothesis that was introduced by Keller (1971). Yet it is unclear whether the plunging flows observed in bedrock rivers are genetically similar to these phenomena.

The potential similarity between the plunging flow regime described in classical hydraulics literature, alluvial pools, and the plunging flow observed in the Fraser canyons warrants investigation of the morphological controls on the initiation and relative strength of velocity inversions. Here I undertake a phenomenological study of the occurrence and strength

of plunging flow in a controlled laboratory experiment in which I vertically or laterally constrained the flow to determine how acceleration of flow immediately upstream of a scour pool affects the occurrence and strength of velocity inversions. The objective is to determine how sill heights, lateral constrictions, scour pool entrance slopes, width-to-depth ratios and discharge affect the occurrence and strength of velocity inversions.

Prototype

In order to reproduce the plunging flow observed in the Fraser canyons, a simple physical model was constructed, based on the geometry of Iron Canyon. This canyon is a vertical-walled bedrock channel, perennially wetted across its width, located 5 km upstream of the confluence of the Fraser and Chilcotin Rivers. This site was selected as a prototype because it exhibits strong velocity inversions (Venditti et al., 2014; Figure 1). Iron Canyon is approximately 1,700 m long with alluvial reaches upstream and downstream. The canyon channel width is 80 m, roughly half of the width of the upstream and downstream alluvial reaches. Iron Canyon has an overall bed slope of 1.1% and the stream-wise bed profile consists of a series of deep scour pools (Figure 1b and c). Entrance bed slopes range between 5° (9%) and 14° (26%). Scour pools coincide with where the channel is laterally constricted (Figure 1d). Lateral constrictions ranged between 29% and 51% at each scour pool entrance relative to the canyon width immediately upstream of the scour pool (Figure 1d).

Observations made at low flow in 2009 show that depths ranged between 5 m and 35 m, and stream-wise flow velocities varied up to 3.5 m/s (Figure 1b). The horizontal and vertical flow structure in Iron Canyon is dominated by a plunging flow structure and velocity inversions at the entrance of each scour pool, drawing high-velocity fluid down towards the channel bed (Figure 1b). The greatest velocities were located in the plunging high-velocity core along scour pool entrance slopes. The velocity inversions are coupled with downward-directed flow along the scour pool entrance slopes (Figure 1c) and there is no upward-directed flow along the bed that would signify the inversion is in fact a vertical recirculation cell.

The prototype is a section of Iron Canyon roughly 500 m downstream from the canyon entrance (Figure 1a) where depth increased from 10.0 m (d1) at the top of the entrance slope to 16.5 m (d2) in the scour pool (Figure 1b) and 51% of the channel width is constricted relative to immediately upstream (Figure 1d). This site was selected as the prototype because a strong inversion was observed along the scour pool entrance slope and the flow was laterally constrained. Flow remained subcritical throughout the prototype. The Froude number ($F_r = \overline{U}/\sqrt{gd}$; g is gravitational acceleration, d is flow depth, $\overline{U}$ is the mean velocity) upstream of the construction was 0.23, at the constriction it was 0.30, and in the scour pool it was 0.09. Other geometric and flow properties of the prototype are provided in Table 1.

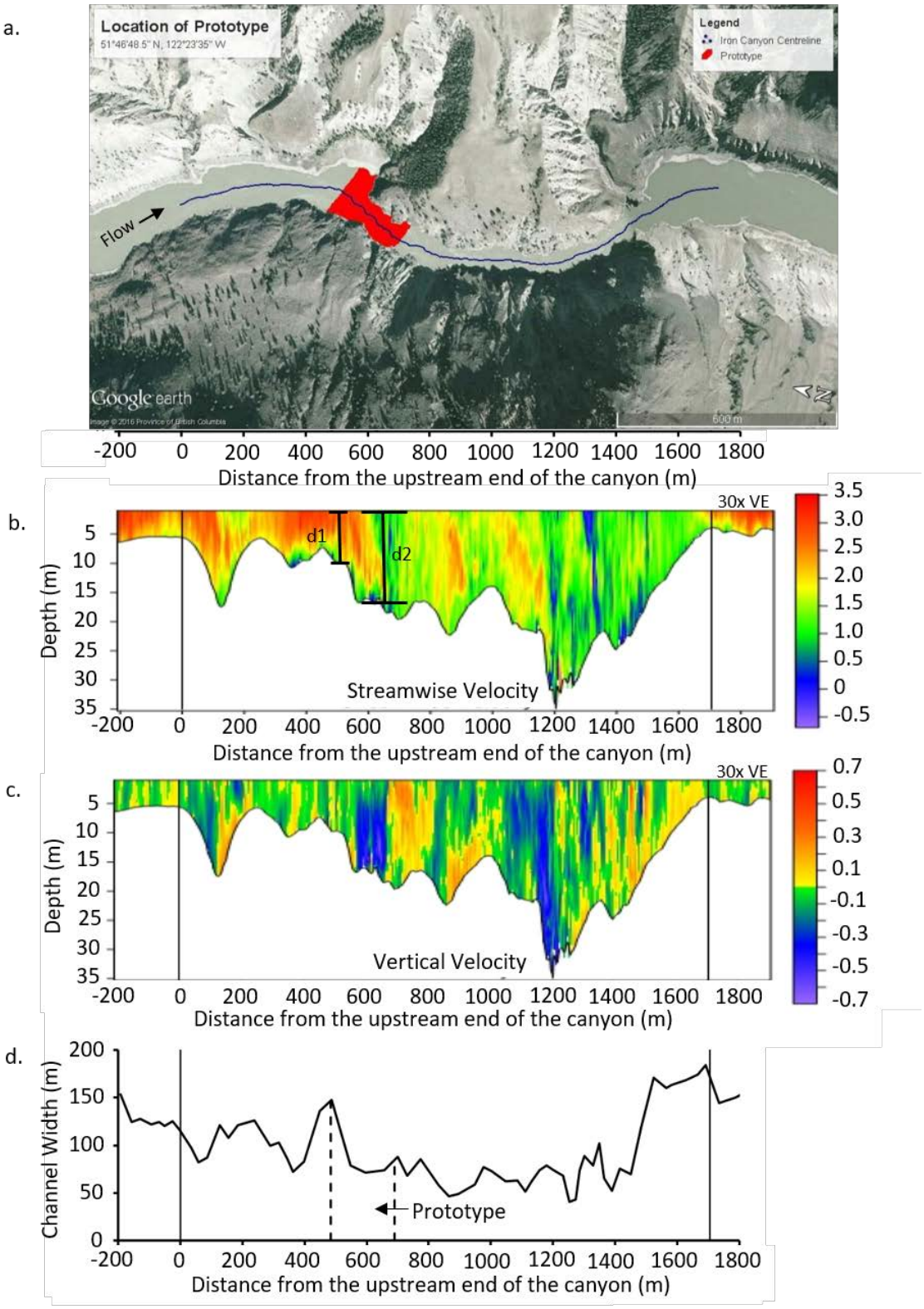

Figure 1. Prototype Location and Flow structure in Iron Canyon. (a) Location of prototype in Iron Canyon. (b) Streamwise and (c) vertical flow velocities through Iron Canyon on September 17, 2009 at a discharge of 830 m^3/s. (d) Channel width through Iron Canyon as measured at the narrowest and widest sections ranged between 41 m and 184 m. Flow depths d1 and d2 are respectively the flow depths at the most prominent constriction and in the downstream scour pool. Flow is from left to right.

Table 1. Geometric and flow properties of prototype and flume model

	Prototype	Flume Model
Constriction (%)	51	20 to 50
Entrance Slope (°)	12	5 to 15
d_1 (m)	10	~0.08
d_c (m)	16.5	0.0455 to 0.068
d_2 (m)	16.5	~0.13
V_1 (m/s)	2.3	0.25 to 0.45
V_c (m/s)	3.0	0.41 to 0.98
V_2 (m/s)	1.0	0.13 to 0.24
Fr_1	0.23	0.33 to 0.57
Fr_c	0.30	0.61 to 1.27
Fr_2	0.08	0.13 to 0.22
Re	10^7	10^4

V_2 and Fr_2 measured downstream of recirculation zone.

Experimental Methods

Flume

Experiments were undertaken in the River Dynamics Research Laboratory at Simon Fraser University using a recirculating flume 480 cm long and 45 cm deep (Figure 2a and b). Width can be adjusted because one of the sidewalls is fixed while the other can be moved to create channel widths of 10 and 20 cm. The head box exit was fitted with a series of metal grates and a 4 cm wide polypropylene fiber filter to diffuse turbulence. A sharp-crested weir at the downstream end of the flume controlled the flow depth. Flow rate was controlled by a variable speed pump.

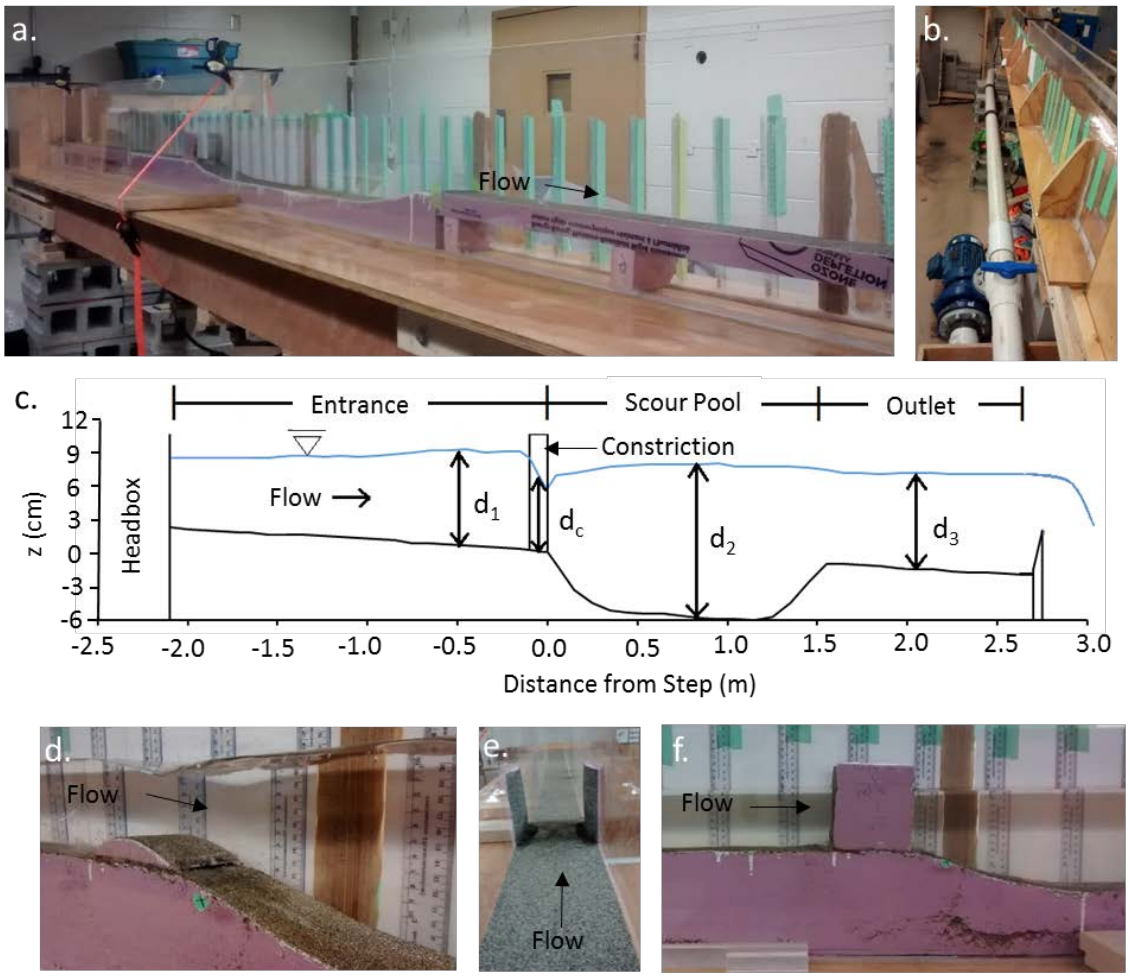

Figure 2. (a) Flume channel and constructed topography looking upstream towards the headbox. (b) Recirculation pump and line. (c) Schematic of channel sections. (d) View of sill. (e) Downstream and (f) side-view of channel with constriction.

The channel bed included a 210-cm-long entrance section, a 150-cm-long canyon scour hole, and a 120-cm-long outlet section (Figure 2c). Flow was perturbed at the entrance to the canyon pool using vertical convex sills (Figure 2d) or lateral convex constrictions (Figure 2e and f), occupying a downstream length of 10 cm. Channel-bed morphologies of different widths and scour pool entrance slopes were carved into C-200 polystyrene rigid styrofoam insulation. The bed was roughened with ~0.5 mm sand fixed to the bed with a light coat of paint.

Experimental Design

The goal was to produce the plunging flow structure observed in the Fraser canyons (Venditti et al. 2014; Figure 1). As such, the experimental design was iterative, and I tried a number of different ways to produce plunging flows. The canyon geometry and flow conditions were scaled to the prototype of Iron Canyon where the pool depth was 1.65x the depth upstream of the scour pool (16.5 m pool depth; 10.0 m approach depth). The experimental entrance and outlet water depths were set to ~8 cm and the pool level was 5 cm below the entrance and outlet (flow depth of ~13 cm). Scour pool entrance slopes of 5°, 10°, and 15° were used to represent the range of slopes entering pools in Iron Canyon.

I used flows that were fully turbulent in terms of the Reynolds number ($R_e = d\overline{U}/\nu$; ν is kinematic viscosity). I also attempted to use flows that were subcritical in terms of the Froude number, a condition that I was always able to satisfy at the entrance to the canyon, but not always through the channel constrictions or over sills. I initially attempted to match the experimental bed slope to the water surface slope of Iron Canyon (1.1%) but this produced supercritical flow through the canyon entrance. The flume slope was then reduced to achieve uniform flow conditions at the entrance and outlet sections. I attempted to match the entrance Froude number of Iron Canyon (0.23) to the entrance to the experimental canyon by adjusting discharge, but those conditions did not produce plunging flow. Therefore, the Froude scaling was relaxed, only requiring the flow to be subcritical along the entrance to the experimental canyon (Table 1) and the remainder of our experiments were largely phenomenological in nature.

For both the constrictions and sills, a reference condition was established where the flow was uniform where the entrance and outlet flow depths were equal. For the constrictions, the reference condition was where 35% of the channel width was laterally blocked relative to immediately upstream and entrance depth equalled outlet depth. For this reference condition

using a 15° slope, plunging flow was produced. Subsequent runs incrementally increased (40%, 50%) and decreased (20%, 30%) the width of constrictions to include the range of constricted widths in Iron Canyon and to examine effects of constriction width on occurrence and strength of plunging flow. The constrictions were tested under the same hydraulic conditions as the 35% reference case with a fixed flume slope (0.9%), weir height (4 cm), and discharge (3 L/s). For the sills, the same hydraulic conditions used for constrictions were tested and yielded no reproducible plunging flow. The reference condition was revised such that uniform flow conditions occurred with 8-cm water depth at both the entrance and outlet without a sill in place by adjusting weir height and discharge, however this produced surface waves through the canyon entrance. Therefore the flume slope was reduced to 0.35%. Weir height and discharge were adjusted to 2.5 cm and 4.6 L/s, respectively, to achieve uniform flow conditions of 8 cm water depth at both the entrance and outlet. Sill heights were then incrementally increased to produce plunging flow with the reference conditions.

Experimental Procedure

In order to explore the effect of flow constriction on the occurrence and strength of velocity inversions, I used different sill heights and constriction widths placed at the top of the scour pool entrance slope. Tables 2 and 3 show the canyon geometry and flow conditions used for the experimental tests. I varied the sill height from no sill to 18%, 21%, 25%, and 28% of the entrance depth using an entrance slope of 15°, a discharge of 4.7 L/s, and 10-cm-wide channel (Table 2). Further tests using sills and different pool entrance slopes, channel widths, and discharge were discontinued because the flows over the sills were consistently supercritical, a condition not observed in the Fraser canyons. I varied the constrictions so that they occupied 20%, 30%, 35%, 40%, and 50% of the channel width with scour pool entrance slopes of 5°, 10°, and 15° using a fixed discharge of 3 L/s and a channel width of 10 cm. I explored the effect of width-to-depth ratio by comparing the occurrence and strength of inversions in the 10-cm-wide channel using 3 L/s with those in a 20-cm-wide channel using 6 L/s (constant specific discharge), a fixed entrance slope of 10°, and all the constriction widths. I also explored the effect of discharge on plunging flow using discharges of 3 L/s and 6 L/s in the 20-cm-wide channel with a fixed entrance slope of 10° and all the constriction widths.

Three runs were conducted for each set of experiments to identify the level of variation between individual runs and to determine if plunging flow was reproducible. For each run, 0.1 mL of rhodamine dye was injected using a syringe 5 cm upstream of the constriction or sill and

approximately 1 cm below the water surface. Nine photographs were taken for each run at three frames per second to capture dye diffusion into the scour pool. I quantified flow velocities along a 1-m-length of the entrance region to the experimental canyon using a series of timed rhodamine dye injections at 0.6 h. Entrance flow velocities were used in conjunction with depth readings at every 0.1 m of channel length to quantify hydraulic conditions and to quantify flow velocities above sill crests or through constrictions.

Data Analysis

MatLab and Analyzing Digital Images (ADI) software were used to extract the coloured dye component from the images and derive profiles of relative dye concentration from the processed images (Figure 3). Dye profiles illustrate the dye colour intensity at pixel-scale. Dye profiles were produced by averaging among the replicates within the full depth of flow and at 5 cm increments from the injection point up to 66 cm downstream of the step, depending on the length of the entrance slope. The horizontal exaggeration was reduced consistently among all dye profiles to avoid overlap among successive profiles. Profiles reflect the vertical displacement of dye between the injection point and entry into the scour pool. If the dye followed along the water surface upon entry to the pool, there was no velocity inversion. However, if the dye descended towards the bed upon entry to the pool, then I judged a velocity inversion to occur. Here, the strength of inversion for each dye profile is defined by the relative depth where the maximum dye concentration occurs.

Table 2. Experimental conditions for sills

Run #	Sill Height		Ent. S	w	w/d_1	Q	Depth				Velocity			Froude #			Strength
	cm	H/d_c %	°	cm		L s^{-1}	d_1 cm	d_c cm	d_2 cm	d_3 cm	V_1 cm s^{-1}	V_c cm s^{-1}	V_2 cm s^{-1}	Fr_1	Fr_c	Fr_2	
S1	1.60	18	15	10	1.17	4.6	8.7	5.9	13.8	8.0	52	77	33	0.56	1.01	0.28	n/a
S2	1.85	21	15	10	1.15	4.6	8.8	5.6	13.8	8.0	51	81	33	0.55	1.09	0.28	mod.
S3	2.25	25	15	10	1.13	4.6	9.0	5.4	13.7	8.0	50	84	33	0.54	1.15	0.29	mod.
S4	2.65	28	15	10	1.08	4.6	9.4	5.5	13.7	8.0	48	82	33	0.50	1.12	0.29	mod.

V_1 and V_c correspond to d_1 and d_c. Fr_1 and Fr_c correspond to d_1 and d_c. V_2 and Fr_2 measured downstream of recirculation zone.

Table 3. Experimental conditions for constrictions

Run #	Constriction Width		Ent. S	w	w/d_1	Q	Depth				Velocity			Froude #			Strength
	cm	%	°	cm		$L\ s^{-1}$	d_1 cm	d_c cm	d_2 cm	d_3 cm	V_1 $cm\ s^{-1}$	V_c $cm\ s^{-1}$	V_2 $cm\ s^{-1}$	Fr_1	Fr_c	Fr_2	
C1	1.0	20	15	10	1.4	3	7.1	6.2	12.8	8.1	42	60	23	0.50	0.78	0.21	n/a
C2	1.5	30	15	10	1.3	3	7.8	6.5	12.8	8.1	38	66	23	0.43	0.83	0.21	mod.
C3	1.8	35	15	10	1.3	3	8.0	6.7	12.8	8.1	37	70	23	0.42	0.86	0.21	strong
C4	2.0	40	15	10	1.2	3	8.2	6.7	12.6	8.0	36	75	23	0.40	0.92	0.21	strong
C5	2.5	50	15	10	1.1	3	8.9	6.8	12.5	7.9	33	88	24	0.36	1.08	0.21	strong
C6	1.0	20	10	10	1.4	3	7.3	6.3	13.3	8.3	40	60	22	0.48	0.76	0.19	n/a
C7	1.5	30	10	10	1.3	3	8.0	6.6	13.3	8.3	37	65	22	0.42	0.81	0.19	mod.
C8	1.8	35	10	10	1.2	3	8.3	6.6	13.3	8.2	36	71	22	0.39	0.88	0.19	mod.
C9	2.0	40	10	10	1.2	3	8.4	6.5	13.2	8.2	35	77	22	0.39	0.96	0.20	strong
C10	2.5	50	10	10	1.1	3	9.3	6.7	13.0	8.0	32	90	23	0.33	1.10	0.20	strong
C11	1.0	20	5	10	1.5	3	6.7	5.6	12.4	8.2	44	67	24	0.54	0.90	0.22	n/a
C12	1.5	30	5	10	1.4	3	7.3	5.8	12.4	8.1	40	74	24	0.48	0.98	0.22	weak
C13	1.8	35	5	10	1.3	3	7.7	5.9	12.4	8.2	38	79	24	0.44	1.04	0.22	mod.
C14	2.0	40	5	10	1.3	3	7.9	6.0	12.3	8.1	37	83	24	0.42	1.09	0.22	strong
C15	2.5	50	5	10	1.1	3	8.8	6.1	12.2	8.0	34	98	24	0.36	1.27	0.22	strong
C16	2.0	20	10	20	4.2	3	4.8	4.6	11.1	6.5	31	41	13	0.45	0.61	0.13	n/a
C17	3.0	30	10	20	4.1	3	4.9	4.8	10.9	6.5	30	45	14	0.43	0.65	0.13	n/a
C18	3.6	35	10	20	3.9	3	5.1	4.8	10.9	6.5	29	48	14	0.41	0.70	0.13	n/a
C19	4.0	40	10	20	3.8	3	5.3	4.8	11.0	6.5	28	52	13	0.39	0.76	0.13	weak
C20	5.0	50	10	20	3.4	3	5.8	4.8	10.9	6.5	25	63	14	0.34	0.91	0.13	weak
C21	2.0	20	10	20	3.1	6	6.5	5.9	13.1	8.2	45	64	23	0.57	0.84	0.20	n/a
C22	3.0	30	10	20	2.9	6	7.0	6.2	12.9	8.2	42	69	23	0.51	0.89	0.20	n/a
C23	3.6	35	10	20	2.7	6	7.4	6.3	12.8	8.2	40	73	23	0.47	0.93	0.21	weak
C24	4.0	40	10	20	2.6	6	7.8	6.4	12.9	8.2	38	78	23	0.43	0.99	0.20	mod.
C25	5.0	50	10	20	2.4	6	8.5	6.7	12.8	8.1	35	90	23	0.38	1.10	0.21	strong

V_1 and V_c correspond to d_1 and d_c. Fr_1 and Fr_c correspond to d_1 and d_c. V_2 and Fr_2 measured downstream of recirculation zone.

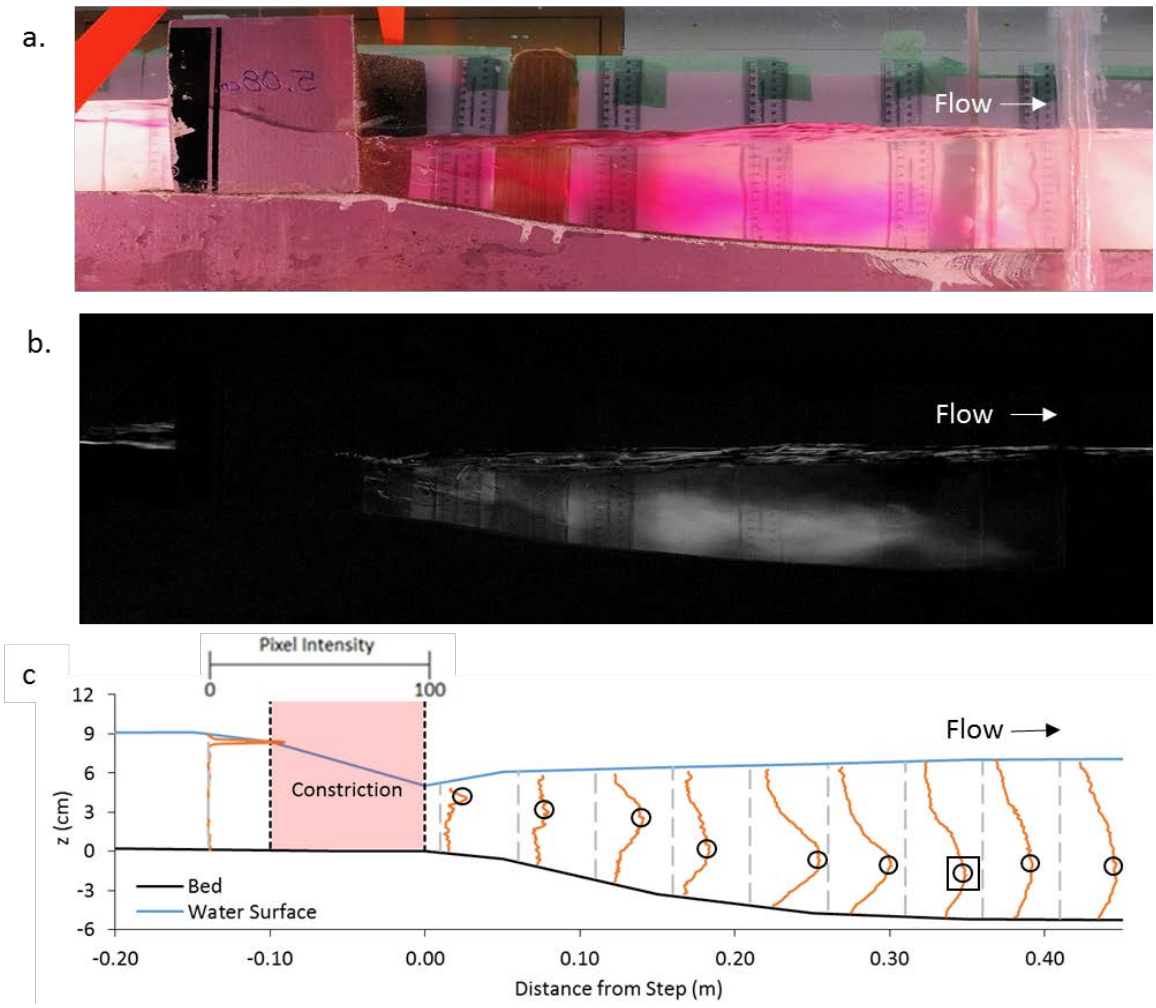

Figure 3. Image analysis of a dye injection into a model canyon. (a) Raw image. (b) Image processed by extracting dye colour component from raw image. (c) Dye profiles calculated by averaging dye colour intensity for each pixel among 3 runs and at 5 cm increments downstream from the step. All panels show plunging flow with a 50% constriction, 20-cm-channel width, 10° entrance slope and discharge of 6 L/s. Vertical dashed lines represent a dye concentration of 0. Circles represent maximum dye concentration per profile. Square represents the deepest relative flow of maximum dye concentrations.

Results

Channel morphology and discharge influenced the occurrence and strength of velocity inversions. Tables 2 and 3 summarize the mean range of flow and hydraulic conditions with the use of all sills and constrictions, respectively, including those that were successful and unsuccessful in producing the plunging flow structure. The strength of the velocity inversion was assessed from processed images and was categorized as 'no inversion', 'weak', 'moderate', or 'strong' (Figure 4), depending on depth of the maximum dye concentration, expressed as percentage of total depth (no inversion is <30%; weak is 30% to 45%; moderate is 45% to 60%; strong is >60%). Assessment of the strength of velocity inversions excluded dye profiles that were relatively uniform in concentration (where the maximum pixel intensity within a profile did not exceed 2x the minimum pixel intensity) and profiles that retained less than half the pixel intensity relative to the injection point.

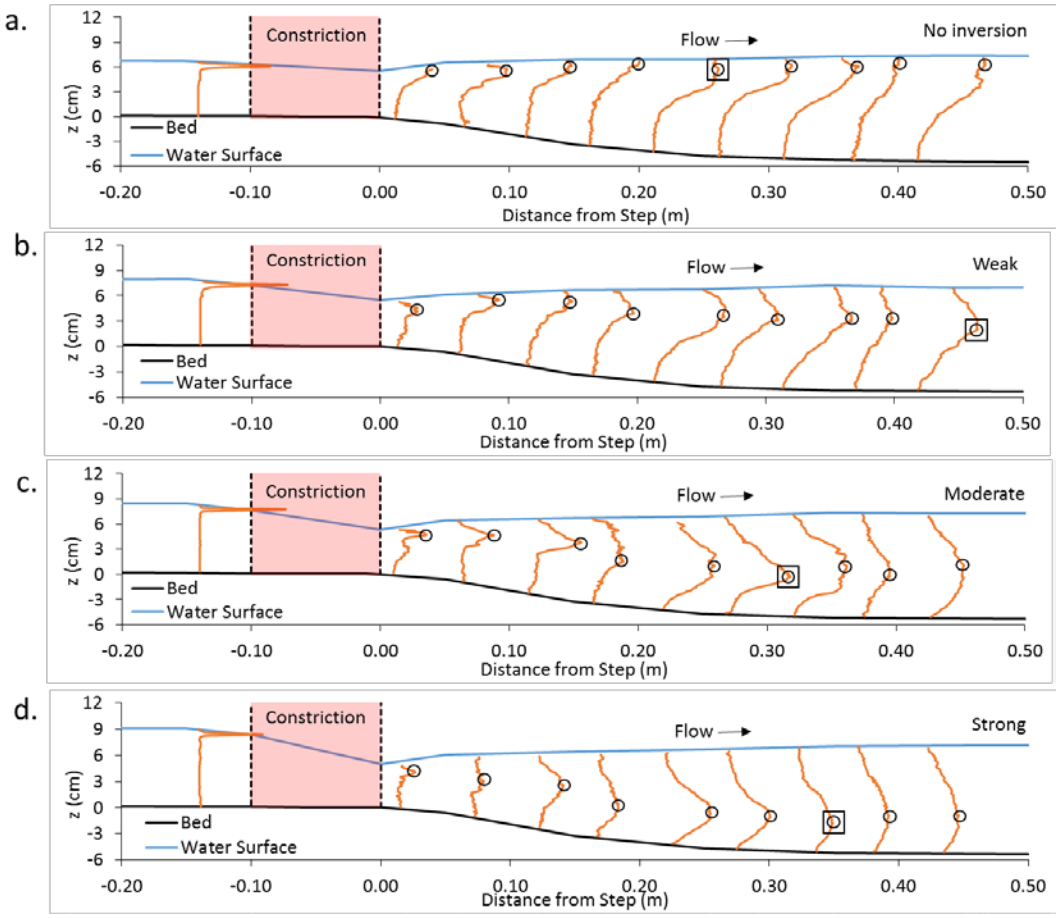

Figure 4. Dye concentration profiles of (a) no velocity inversion using a 20% constriction, (b) weak inversion using a 35% constriction, (c) moderate inversion using a 40% constriction, and (d) strong inversion using a 50% constriction. All panels show profiles with a 20 cm channel width, 10° entrance slope, and discharge of 6 L/s.

Effect of Sill Height

Dye pathways, showing the path of the maximum dye concentration, reveal that sill height influences the occurrence of velocity inversions when the sill is greater than 18% to 20% of the entrance flow depth (Figure 5). A sill height that occupied 18% of the entrance water depth did not produce plunging flow. However, using the same flow conditions, sill heights that occupied 21%, 25%, and 28% of the entrance water depth were successful in producing a moderate velocity inversion (Table 2). Therefore, sill heights needed to occupy a sufficient proportion of the depth for an inversion to occur. Enhanced backwater with taller sills may explain why the strength of plunge was identical among all sill heights that successfully produced a plunge. Prior observations in this investigation identified that strong plunging flow was possible using shorter sills with less discharge. The percentage depth of the maximum dye concentration increases asymptotically to between 50% and 55% of the depth (Figure 6a). Dye concentration profiles became nearly uniform at 31 cm downstream from the step.

I calculated the Froude number for flow over the sills and recognized flow was always supercritical (Fr ranged from 1.1 to 1.2) if plunging flow was produced, suggesting that these were a type of submerged hydraulic jump. Froude numbers were nearly identical, likely due to enhanced backwater with increased sill height. Flow upstream and downstream of these sills was subcritical, and a surface roller vortex formed at the toe of each sill. Approach Froude numbers for these sills were minimally reduced with an increase in sill height, ranging from roughly 0.5 to 0.6. Froude numbers for the sill that was unsuccessful in producing an inversion and a hydraulic jump were 0.6 along the entrance and 1.0 at the sill crest. The supercritical flow over sills that yielded an inversion leads to the interpretation that an inversion occurs only if a submerged hydraulic jump was formed immediately downstream of the step. If a submerged hydraulic jump was formed, a velocity inversion occurred. If a submerged hydraulic jump was not formed, an inversion did not occur. Since I was unable to produce velocity inversions in subcritical flow conditions that represent the flow conditions of our prototype, I discontinued the sill runs.

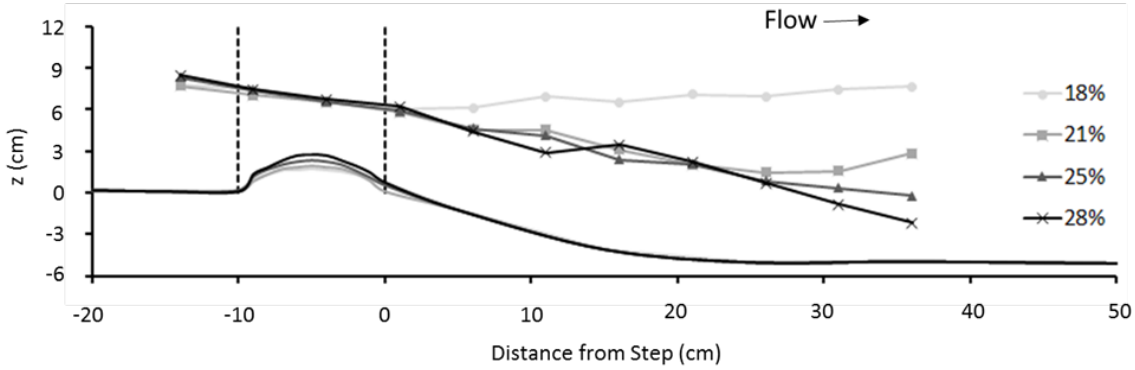

Figure 5. Pathway of maximum dye concentrations for each sill height with a 10-cm channel width, 15° entrance slope and discharge of 4.7 L/s.

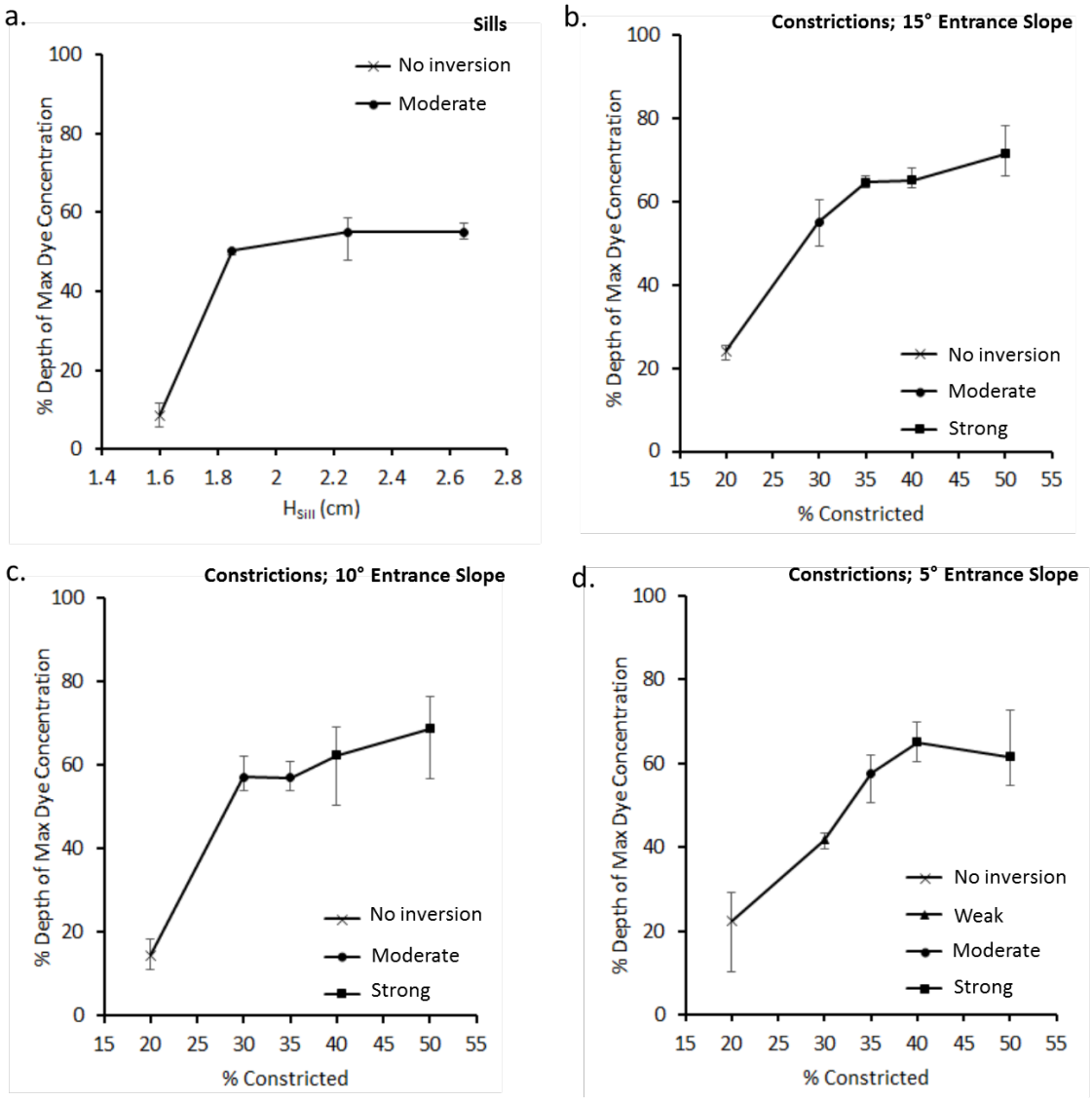

Figure 6. Strength of inversion by (a) sill height, (b) constrictions with 15° entrance slope, (c) 10° entrance slope, and (d) 5° entrance slope. Error bars indicate range of individual runs.

Effect of Channel Constriction

Dye pathways for the channel constrictions reveal that, with the exception of the 20% constriction, some form of plunging flow developed (Figure 7a). The reference condition for the constrictions (where 35% of the channel width is constricted and using a 15° scour pool entrance slope) produced a strong inversion (Table 3). Maximum dye concentration was located at 65% of the depth and ranged between 21 and 26 cm downstream into the pool. Strong inversions were also produced using the 40% and 50% constrictions. Maximum dye concentrations were located at 65% and 71% of the depth using the 40% and 50% constrictions, respectively. A moderate-strength inversion was produced using the 30% constriction and no inversion occurred using the 20% constriction.

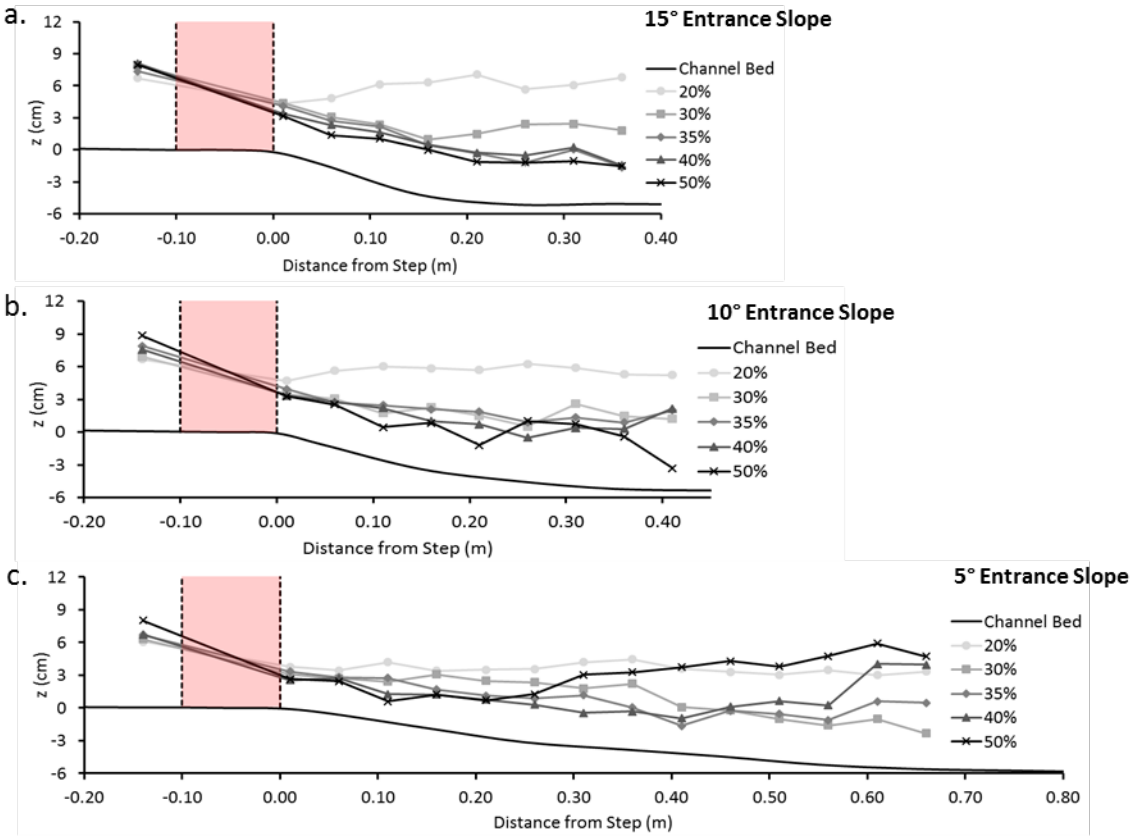

Figure 7. Pathway of maximum dye concentrations for (a) 15° entrance slope, (b) 10° entrance slope and (c) 5° entrance slope. Channel is 10 cm wide and discharge is 3 L/s. Flow is left to right.

Channel constriction affects the occurrence and strength of velocity inversions into scour pools. Constrictions that occupy a greater proportion of the channel width yield stronger inversions. This was evident among all entrance bed slopes. The percent depth at which the maximum dye concentration occurs increases non-linearly with the percent constriction, and

may be approaching an asymptote (Figure 6b), as observed for sills. For each occurrence of plunging flow, a vertical recirculation cell developed near the water surface, from the downstream end of the constrictions where flow depth was at a minimum. The recirculation region extended downstream above the scour pool entrance slope or above the horizontal plane of the scour pool. Observations of the recirculation zone were not sufficient to characterize its shape or extent, but did reveal its presence or absence. A recirculation region was absent when plunging flow was not produced.

Effect of Scour Pool Entrance Slope

Dye pathways reveal that the slope of the scour pool entrance does not influence the occurrence of velocity inversions (Figure 7). Each experimental entrance slope for the 10 cm channel supported velocity inversions using constrictions of 30%, 35%, 40%, and 50% of the channel width but did not support velocity inversions using a 20% constriction (Table 3). The strength of the velocity inversions increased slightly with entrance slope (Table 3). This effect was most apparent with the 30% constriction where the strength increases from weak at 5° to moderate at 10° and 15° entrance slopes. This also occurs for the 35% constriction where strength increases from moderate for 5° and 10° entrance slopes to strong at a 15° entrance slope. There does not appear to be any difference in the relation between the percent depth of the maximum relative dye concentration and the percent constriction (Figure 6b, c, and d). All increase towards an asymptote that is ~60% of the flow depth.

Effect of Discharge

Dye pathways reveal that discharge influences the occurrence of velocity inversions (Figure 8). In the 20-cm-wide channel, a discharge of 3 L/s was successful in producing velocity inversions with 40% and 50% of the channel width constricted, and a discharge of 6 L/s was successful in producing velocity inversions with 35%, 40%, and 50% of the channel width constricted (Table 3). The strength of velocity inversions was enhanced with discharge (Figure 9). This effect was most apparent with the 50% constriction that produced a weak inversion using a discharge of 3 L/s and a strong inversion using a discharge of 6 L/s. Also, the 40% constriction produced a weak inversion using a discharge of 3 L/s and a moderate inversion using a discharge of 6 L/s. There is a large difference in the % depth where the maximum dye

concentration occurs increasing with the percent constriction towards an asymptote that is ~35% and ~70% of the flow depth using a discharge of 3 L/s and 6 L/s, respectively.

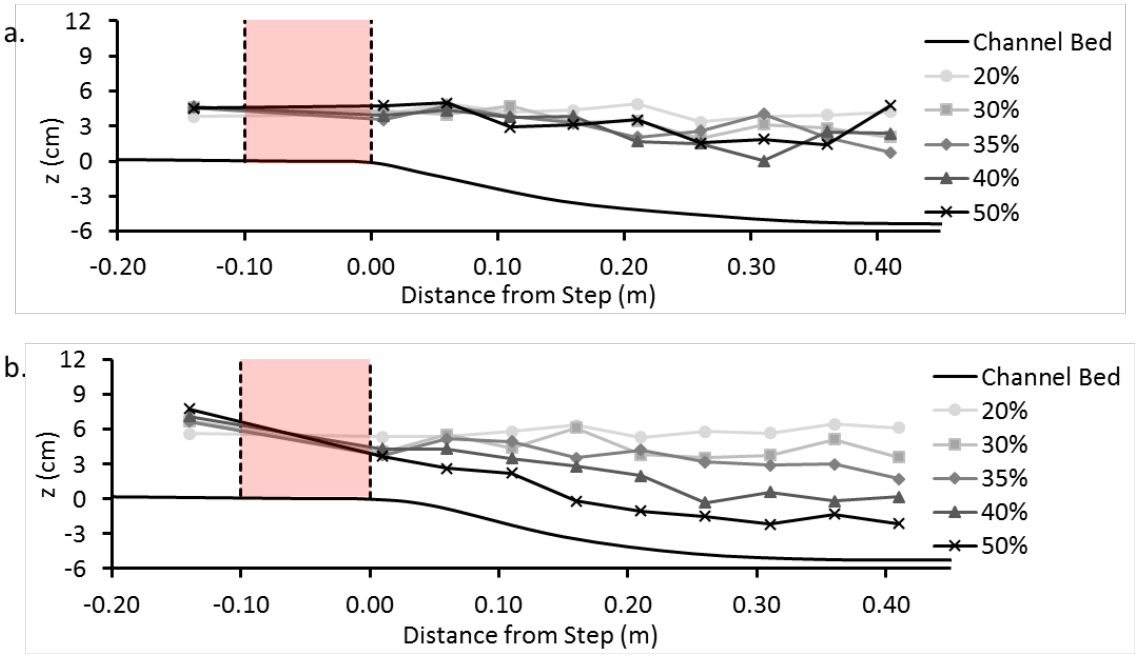

Figure 8. Pathway of maximum dye concentrations with a 20 cm channel width and discharge of (a) 3 L/s and (b) 6 L/s. Flow is left to right.

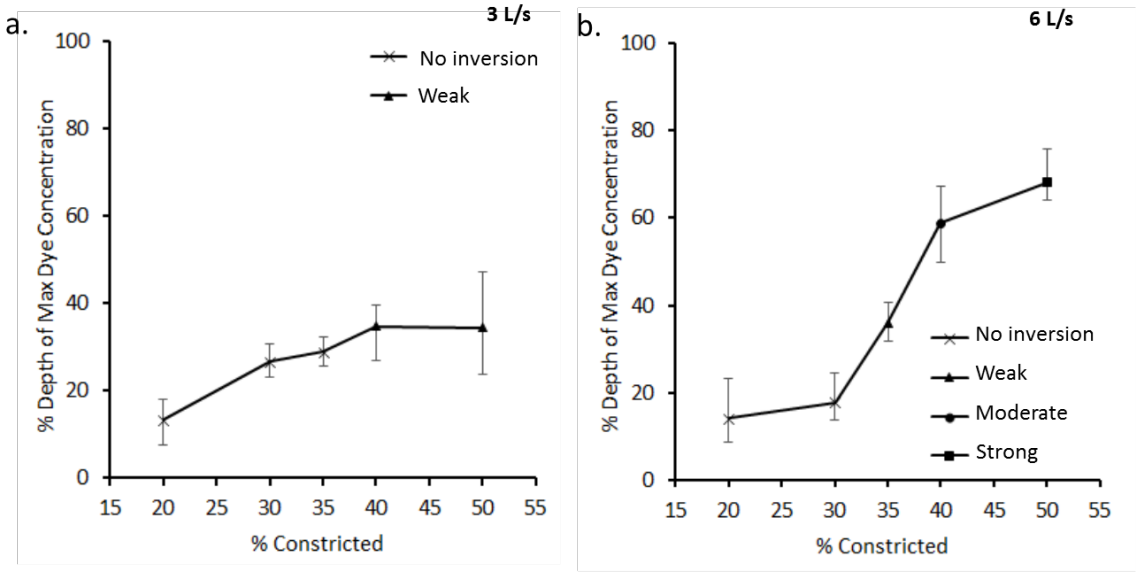

Figure 9. Strength of inversion with a 20 cm channel width and discharge of (a) 3 L/s and (b) 6 L/s. Error bars indicate range of individual runs.

Effect of Width-to-Depth Ratio

Dye pathways reveal that width-to-depth ratio, defined here by the full channel width and the maximum pool depth, had a minimal influence the occurrence and strength of velocity inversions (Figure 7b and 8b). The width-to-depth ratio was established by maintaining a specific discharge of 0.03 cm^2/s between the 10-cm (3 L/s) and 20-cm (6 L/s) wide channels, providing width-to-depth ratios of 0.8 and 1.6, respectively. Velocity inversions were produced with 30% to 50% of the channel width constricted in the 10 cm wide channel, and with 35% to 50% of the channel width constricted in the 20 cm wide channel (Table 3). Overall, the strength of velocity inversions was greater for a width-to-depth ratio of 0.8 (Table 3). However, considering all runs in this investigation that used different specific discharge values, I found that plunging flows occurred over the same range of width-to-depth ratios (0.8 to 1.8) as non plunging flows. This consistency suggests that plunging flow can occur in a range of width-to-depth ratios and is governed by the channel width that is constricted, entrance slope, and discharge.

When maintaining a specific discharge of 0.03 cm^2/s between the 10-cm and 20-cm wide channels, there appeared to be a difference in the relation between the percent depth of the maximum relative dye concentration and the width-to-depth ratio. The greatest difference was observed with the 35% constriction where the maximum dye concentration was 62% of the depth in the 10-cm-wide channel (Figure 6c) and 36% of the depth in the 20-cm-wide channel (Figure 9b). The 50% constriction yielded inversions in the 10-cm and 20-cm-wide channels of nearly identical strength.

Discussion

Characteristics of plunging flow and analogues

There are two analogues to the flows in the experiments that shed light on flow processes: flow in alluvial pools and flow over submerged broad crested weirs. The experiments resemble flow through riffle-pool sequences. Keller (1971) proposed a velocity reversal hypothesis that is responsible for the maintenance of riffle-pool morphologies: At low flows, higher velocities and shear stresses occur over riffles than in pools; and at high flows, the near-bed velocities and shear stresses in pools are greater than those over riffles. There has been much debate over the velocity reversal hypothesis (c.f. Clifford and Richards, 1996; MacWilliams et al., 2006). Tests of the hypothesis have not definitively rejected or confirmed it. Yet, efforts to test this hypothesis show flow converges along the centreline in convectively decelerating flow into a pool (MacVicar and Rennie, 2012; MacVicar et al., 2013; MacVicar and Best, 2013). This concentration of flow toward the centreline produces a secondary flow structure where there is downward directed flow along the channel centreline and upwelling along the sidewalls (MacVicar and Rennie, 2012). The initial adjustment in flow pattern during convective decelerating flow is generated by a change in the streamwise pressure gradient, in which changes to the velocity gradient and turbulence production spread over the entire boundary layer (Smits and Wood, 1985). The presence of a flow constriction at the head of a pool enhances flow concentration (Booker et al., 2001; Wilkinson et al., 2004; MacWilliams et al., 2006; Thompson, 2006; Sawyer et al., 2010). Thompson et al. (1996, 1998, 1999) have shown constrictions that are capable of forming lateral recirculation eddies are particularly effective at concentrating flow by reducing the effective cross-sectional area of downstream flow. Currently, there is no documented evidence of plunging flows in riffle-pool sequences, although near-uniform velocity profiles have been observed along a pool exit slope in a straight flume channel (MacVicar and Rennie, 2012) and observations by MacVicar and Best (2013) suggest a weak plunge may have occurred in some of their experiments (see their Figure 5).

In the experiments, sills and lateral constrictions produced flow convergence at the head of the pool. Plunging flow occurred when there was sufficient convergence, causing downward-directed flow to be concentrated along the channel centreline into the scour pool. Occurrences of plunging flow coincided with the presence of a vertical recirculation vortex near the water surface, anticlockwise in direction, in the upstream region of the pool. This vortex reduces the

effective cross-sectional area of downstream flow. The occurrence and strength of plunging flow was enhanced with channel morphologies that supported greater rates of convective deceleration into the pool, including sills that increasingly constrict the flow vertically with height (Figure 6a), constrictions that occupy a greater proportion of the channel width (Figures 6b, c, and d), steeper entrance slopes (Figure 6b, c, and d), and smaller width-to-depth ratios (Figure 9). These findings suggest that the rate of convective deceleration into a pool controls the occurrence and strength of plunging flow.

Channel morphologies that supported greater rates of convective deceleration into the pool yielded steeper water surface slopes between the upstream and downstream ends of the constrictions. Water surface slopes provide the driving energy for flow through a constriction, and are enhanced during high flows and with the amount of flow constriction (Kieffer, 1989). Thompson et al. (1999) also observed steep water surface gradients upstream of a constriction that enhanced the flow velocity into the pool. According to Thompson et al. (1998), the presence of a constriction is of primary importance to the development of a jet in a pool because the constriction creates backwater, a high water surface slope, and high-velocity flow entering the pool. In the experiments, the water surface gradient through the constriction influenced the occurrence and strength of plunging flow that reflects the driving energy of the flow through the constriction and into the scour pool. The strength of plunging flow increases with constriction width because greater constriction super-elevates the water surface upstream of the constriction, which plunges into the scour pool.

A more direct analogue to the velocity inversions in bedrock channels can also be found in the literature on flow over broad crested weirs (Escande, 1939; Kindsvater, 1964; Tracy, 1967; Borland-Coogan, 1980; Leutheusser and Birk, 1991; Fritz and Hager, 1998; Wang et al., 2010). Escande (1939) showed that when a flow is accelerated over a broad crested weir, there are four distinct types of flow regimes that may occur, the emergence of which depends on the elevation of the water surface downstream of a weir (tailwater depth) relative to the approach depth upstream of the weir. The four flow regimes include:

1) Type A, classic hydraulic jump with the water surface downstream of the weir below the weir crest level;

2) Type B, plunging jet flow with the main flow directed along the boundary with a surface roller vortex;

3) Type C, surface wave flow with the main flow along the free surface and a bottom recirculation zone; and,

4) Type D, surface jet flow that is analogous to Type C flow and a nearly horizontal water surface.

Type A flow always occurs when the downstream water level is less than the weir height (i.e. the weir is not drowned), and may occur as drowned-out jumps in sloping channels where flow plunges into a downstream pool below a steep slope (Chow, 1959). Alternatively, the downstream water level is greater than the weir height for the submerged flows of Type B, Type C and Type D flows (Wang et al., 2010).

The different flow regimes can be distinguished using the relative submergence of the weir, which in the present experiments can be calculate as:

$$y_p = (d_2 - z_s)/d_1$$

where z_s is the scour depth. If y_p < 0, Type A flow will occur. If 0 < y_p < 1 then Type B plunging flow will occur. If y_p > 1 then Type C, bottom recirculating flow, or Type D, surface jet flow, will occur (c.f. Escande, 1939; Fritz and Hager, 1998). I found that plunging flows in the present experiments are properly characterised where y_p > 1, with the exception of Runs S1, C18 and C22 that had y_p values of 0.98, 0.99, and 0.99, respectively, even though plunging flow was not produced. There are other metrics to identify the transition between Type B plunging flow and Type C bottom recirculating flow regimes (e.g. Fritz and Hager, 1998) but they incorporate the flat weir crest length, for which there is no analogue in the present experiments. Therefore I cannot apply them to the data without making arbitrary decisions about what constitutes weir crest length for sills and constrictions.

Differences in the flow regime between the model and the prototype

The flume experiments successfully reproduced velocity inversions that are in many ways similar to those observed in the Fraser canyons, although there are fundamental differences between the model and prototype that should be noted. Flows remained subcritical in Iron Canyon (Table 1), however in some of the experiments, velocity inversions were

produced when flow through the constriction crest was supercritical. Flow remained subcritical upstream of the constriction crest in all of the runs, ranging from 0.3 to 0.9 (Figure 10a), but Froude numbers measured at the constriction crest (Fr_c) ranged from 0.8 to 1.2 for constrictions that produced an inversion (Figure 10b). A weak positive relation was observed between the Froude number at the constriction crest and strength of the inversion in which greater Froude numbers at the constriction crest resulted in stronger inversions (Figure 10b); however, there were some exceptions. For instance, supercritical flow did not produce a velocity inversion in Runs C11 and C21 where 20% of the channel was constricted. Those runs with supercritical flow at the constriction crest yielded strong, moderate, and no velocity inversions. It is useful to note that subcritical flow at the constriction crest also yielded strong, moderate, weak, and no velocity inversions.

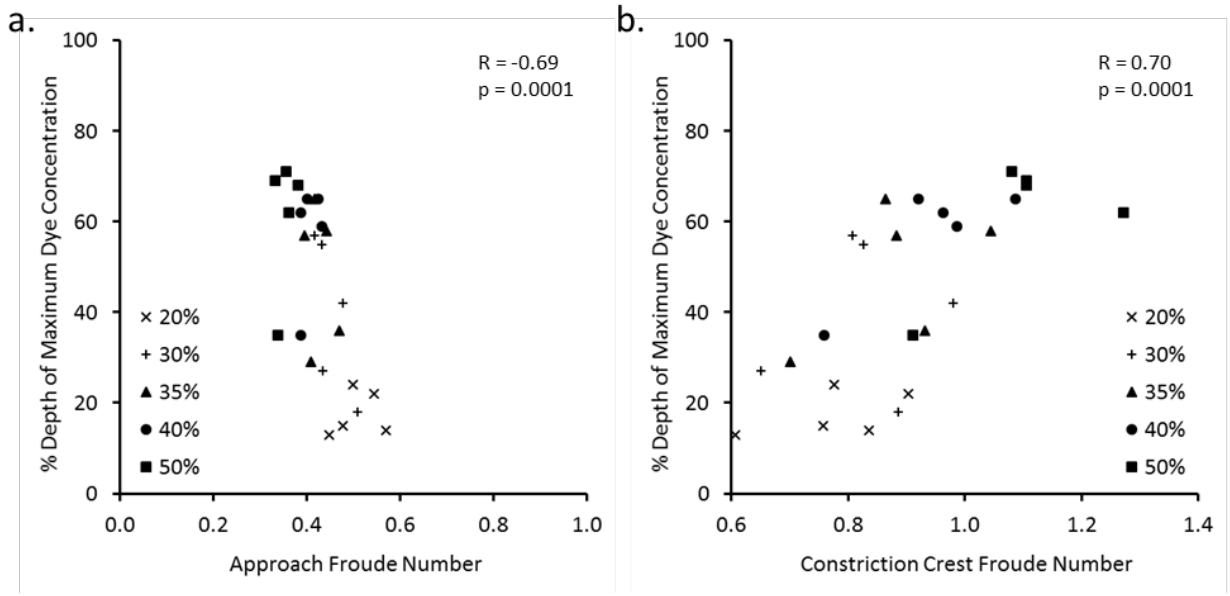

Figure 10. Effect of Froude number at the (a) entrance and (b) constriction crest on the strength of velocity inversions. R is the Pearson product-moment correlation coefficient.

A weak inverse relation was observed between the Froude number upstream of the constriction crest (Fr_1) and strength of the inversion in which smaller approach Froude numbers resulted in stronger inversions (Figure 10a). With wider constrictions, there were more pronounced backwater effects in the flow approaching the constrictions, which super elevated the water surface (smaller y_p values) and enhanced the plunging flow. For example, the 50% constrictions produced the smallest approach Froude numbers despite having the strongest velocity inversions overall. An exception is Run C20 that produced a weak velocity inversion and yielded one the smallest approach Froude Number (0.36) of the constrictions.

While the plunging flows I examined have typically been examined in supercritical flows over weirs, they have been documented in subcritical flows as well. Wang et al. (2010) reported Froude numbers over a trapezoidal weir between 0.66 and 0.86 that produced Type B plunging flow in which the generation of Type B flow was highly dependent on Froude number and downstream water surface elevation. In the experiments, Froude numbers at the constriction crest for non-occurrences of velocity inversions ranged from 0.7 to 1.1, although Wang et al. (2010) encountered a range of 0.40 to 0.66 above the weir that did not produce Type B plunging flow. This difference between our observations and those of Wang et al. (2010) is likely due to differences in submergence ratios.

According to Kieffer (1989), flows are subcritical when there is a relatively small difference in head between upstream and downstream of the constriction (i.e. if the difference is less than approximately one-third of the head upstream of the constriction), and can reach critical or supercritical flow conditions through the constriction when the water surface gradient becomes steeper. If the constriction is too severe to accommodate all of the discharge, enhanced backwater increases the specific head upstream of the constriction over that downstream of the constriction, and permits a greater discharge per unit area (Kieffer, 1989). These findings support the observation of subcritical, critical and supercritical flow conditions through constrictions, in which velocity inversions were produced.

Differences from the prototype induced by model simplification

Although the channel morphology used in this flume investigation is a simplified form of Iron Canyon (matching entrance slopes; ratio of pool depth to entrance depth; constricted at the top of the step; lateral flow convergence at constriction), there are differences in their morphology and character that influence flow processes. The plunging flow reproduced in this investigation resembles the Type B flow regime that typically has a surface recirculation region. The experiments also typically exhibited upstream movement of flow that occupied the full channel width near the water surface. The plunging flow structures observed by Venditti et al. (2014) did not develop upstream-moving flow along the channel centreline near the water surface. In the Fraser canyons, upwelling occurred along the canyon walls to counterbalance the downward movement of flow into the scour pool, resulting in large-scale boils (up to tens of metres in diameter) at the surface. These boils appeared to pulse intermittently, likely due to

readjustment of the decelerating highly-turbulent flow. Venditti et al. (2014) suspected that upwelling along the channel walls and lateral convergence of flow at the water surface during deceleration into the pool resulted in relatively low-speed, highly-turbulent fluid at the water surface in the channel centre downstream of the constriction.

The lack of a recirculation region along the channel centreline in the Fraser canyons may also be attributed to the irregularity of localised channel width that may allow slower or upstream-moving flow to be directed along the channel walls in wider zones. Additionally, greater roughness along the channel walls than the bed may direct flow toward the centre of the channel. Contrarily, the smooth channel walls and fixed width in the flume channel do not represent the wall roughness in Iron Canyon and allow downstream-moving flow along the channel walls. The rough bedrock walls in the Fraser canyons enhance drag forces and more effectively decelerate flow into the scour pool, whereas the smooth and straight flume channel walls used in this investigation have relatively small drag forces to decelerate flow into the scour pool.

Plunging flow in the Fraser canyons occurred where width-to-depth ratios (defined by mean canyon width and maximum pool depth for each individual plunging flow structure) were small (Venditti et al., 2014). Stream-wise velocities should decline faster in narrower pools than in wider pools due to differences in convective deceleration rates (MacVicar and Best, 2013) and this should increase the strength of plunging flows; however, the experiments have no evidence to support or dispute this relation. In this investigation, the occurrence and strength of velocity inversions increased minimally in smaller width-to-depth ratios (defined by scour pool width and maximum pool depth). I found that water surface gradients through the constriction were steeper in the narrower channel despite using a constant specific discharge value between the two channels. This may be attributed to the minimal difference in the occurrence and strength of velocity inversions. It is likely that the limited length of the lateral constriction in the experiments conditioned this observation. Had I laterally constrained the channel from a wide channel to a narrow channel, that mimicked a transition from an alluvial channel to a canyon and back to an alluvial channel, a more pronounced change may have been observed.

Implications for erosion and morphological evolution in natural bedrock channels

Venditti et al. (2014) hypothesized that the plunging flow phenomenon observed in the Fraser canyons was due to convective deceleration as flow exits the constriction and enters the scour pool, causing high-velocity fluid to plunge below the decelerated flow. This investigation is in agreement with the hypothesis proposed by Venditti et al. (2014) and has shown the occurrence and strength of plunging flow are dependent on discharge and constriction width. Water surface gradients through constrictions, which are a by-product of discharge and constriction width, were reported by Venditti et al. (2014) in the Fraser canyons where plunging flow occurred although the water surface gradients from the 2009 survey are not known well enough to provide accurate values.

Our understanding of feedbacks between hydraulics and channel geometry is incomplete (Thompson and Wohl, 1998; Richardson and Carling, 2005; Sofia et al., 2015). Flow patterns change with stage, and the influence of canyon walls in low width-to-depth ratios where plunging flow was observed may impact flow energy expenditure (Richardson and Carling, 2005). In channels that are laterally constricted and have low width-to-depth ratios, canyon walls may exert a greater influence on flow structures and their associated bedforms. Therefore, in the same manner that bedforms have distinct flow structures through convergence of form in a range of environments (Richardson and Carling, 2005), the plunging flow structure observed in the narrower canyons of the Fraser canyons may be a frequent occurrence in various bedrock channels that are constricted, depending on stage.

The plunging flow structure can be expected to occur in bedrock canyons that constrain the flow laterally with implications for pronounced channel incision and landscape evolution. In canyons that produce plunging flows, incision along the entrance slope will steepen the channel and may thereby promote stronger plunging flow structures and enhanced bed shear stresses. In the same manner, it can be expected that narrower canyons that produce plunging flow beyond the entrance slope have deeper pools. Canyons that produce plunging flow will continue to evolve until morphodynamic equilibrium of the channel is achieved. Hancock et al. (1998) have shown that the effectiveness of channel incision mechanisms is sensitively dependent on flow conditions, in which the process effectiveness scales non-linearly with velocity. In particular, a two-fold increase in mean velocity induced from either local channel narrowing or steepening, can result in a ~2 to 10-fold increase in erosion rates (Hancock et al.,

1998). These estimates highlight the importance of large, rare flow events, although do not account for the plunging flow phenomenon observed recently by Venditti et al. (2014) in the Fraser canyons. Local channel narrowing and steepening is a frequent occurrence in the Fraser canyons, and the occurrence of this flow structure would significantly enhance the estimates of Hancock et al. (1998) through increased bed shear stress. The distribution of bed shear stresses in Iron Canyon was calculated by Venditti et al. (2014) from reach-averaged momentum balance, velocity profiles through the whole water column, and the lower linear portion of the velocity profile below the inversion, identifying a four-fold increase in localised bed shear stress between the canyon entrance and the entrance slope that would substantially enhance predicted erosion rates that assume steady, uniform flow conditions.

Conclusions

A phenomenological investigation was conducted to reproduce the flow fields observed in the Fraser canyons, and to address the influence of morphological controls on the occurrence and relative strength of the plunging flow structure in bedrock canyons. Flume channel morphologies were based on a prototype model of Iron Canyon, where strong plunging flow was observed in reaches that had low width-to-depth ratios and were laterally constrained. I compared the occurrence and strength of plunging flow with sills and constrictions placed at the top of the scour pool entrance slope, using various sill heights, constriction widths, entrance slopes, width-to-depth ratios, and discharge values.

The main results of this investigation are as follows:

1. Supercritical flow over channel spanning sills is necessary to produce velocity inversions and the strength of plunging flow increases with sill height.

2. Velocity inversions can also be produced by laterally constricting the channel. The strength of plunging flow increases with the amount of channel constricted laterally because greater constriction super-elevates the water surface upstream of the constriction, which plunges into the scour pool.

3. Scour pool entrance slope affects the strength of plunging flow by altering the surface area of the channel boundary. The strength of plunging flow increases with steeper scour pool entrance slopes.

4. Discharge affects the strength of plunging flow since the discharge level dictates the amount of flow concentration through the constriction. The strength of plunging flow increases with higher discharge levels.

5. At a fixed specific discharge, the occurrence and strength of plunging flow minimally increases with lower width-to-depth ratios. However, when width-to-depth ratio is not held fixed, plunging flow can occur in a range of width-to-depth ratios and is governed by discharge, entrance slope, and the channel width that is constricted.

6. There is an association between the strength of plunging flow and the Froude number. Plunging flow can be produced in subcritical flows, but the strength of plunging flow increases with the Froude number through a constriction or over a sill.

Plunging flow phenomenon can be produced by a variety of different channel morphologies and flow conditions. The high-velocity core induced by plunging flows greatly enhances the potential for incision to occur along the channel bed and is an extreme departure from the assumptions of steady, uniform flow in bedrock incision models. This highlights the

need for improved fluid flow formulations. Parameterization of the flow in incision models needs to account for the plunging flow structures produced in this investigation and those observed in bedrock canyons. Further research is needed to quantify bed shear stresses and incision rates where plunging flow occurs, and improve incision models to account for this process where canyons are laterally constrained at the entrance to a scour pool.

References

Attal, M., Tucker, G. E., Whittaker, A. C., Cowie, P. A., and Roberts, G. P. (2008). Modeling Fluvial Incision and Transient Landscape Evolution: Influence of Dynamic Channel Adjustment. *Journal of Geophysical Research: Earth Surface*, *113*(F3).

Booker, D. J., D. A. Sear, and Payne, A. J. (2001). Modeling Three-dimensional Flow Structures and Patterns of Boundary Shear Stress in a Natural Pool-riffle Sequence, *Earth Surface Processes and Landforms*, 26, pp. 553–576.

Borland-Coogan (1980). Filmspace Productions, *The Drowning Machine* (video).

Braun, J., & Sambridge, M. (1997). Modelling Landscape Evolution on Geological Time Scales: A New Method Based on Irregular Spatial Discretization. *Basin Research*, *9*(1), 27–52.

Chatanantavet, P., and Parker, G. (2009). Physically Based Modeling of Bedrock Incision by Abrasion, Plucking, and Macroabrasion. *Journal of Geophysical Research, 114*(F04018).

Chow, V.T. (1959). Open-channel Hydraulics. New York, McGraw-Hill, 680 p.

Clifford, N. J., and Richards, K. S. (1992). The Reversal Hypothesis and the Maintenance of Riffle-pool Sequences: A Review and Field Appraisal, in *Lowland Floodplain Rivers: Geomorphological Perspectives*, edited by P. A. Carling and G. E. Petts, pp. 43–70, John Wiley, Hoboken, N. J.

Coulthard, T. J., Macklin, M. G., & Kirkby, M. J. (2002). A cellular model of Holocene Upland River Basin and Alluvial Fan Evolution. *Earth Surface Processes and Landforms*, *27*(3), 269–288.

Escande, L. (1939). Recherches Nouvelles sur les Barrages Déversoirs Noyés. *La Technique Moderne*, *31*(18), 617–620 (in French).

Finnegan, N. J., Roe, G., Montgomery, D. R., and Hallet, B. (2005). Controls on the Channel Width of Rivers: Implications for Modeling Fluvial Incision of Bedrock. *Geology*, *33*(3), 229–232.

Fritz, H. M., & Hager, W. H. (1998). Hydraulics of Embankment Weirs. *Journal of Hydraulic Engineering*, *124*(9), 963–971.

Hancock, G. S., Anderson, R. S., and Whipple, K. X. (1998). Beyond power: Bedrock River Incision Process and Form. In *Rivers Over Rock: Fluvial Processes in Bedrock Channels* (pp. 35–60).

Houjou, K., Shimizu, Y., and Ishii, C. (1990). Calculation of Boundary Shear Stress in Open Channel Flow. *Journal of Hydroscience and Hydraulic Engineering, 8*, 21–37.

Howard, A. D. (1994). A Detachment-limited Model of Drainage Basin Evolution. *Water Resources Research*, *30*(7), 2261–2285.

Howard, A. D., and Kerby, G. (1983). Channel Changes in Badlands. *Geological Society of America Bulletin, 94*(6), 739–752.

Kabiri-Samani, A., Ansari, A., and Borghei, S. M. (2010). Hydraulic Behaviour of Flow over an Oblique Weir. *Journal of Hydraulic Research*, *48*(5), 669–673.

Kean, J. W., and Smith, J. D. (2004). Flow and Boundary Shear Stress in Channels with Woody Bank Vegetation. In S. J. Bennett, and A. Simon (Eds.), *Riparian Vegetation and Fluvial Geomorphology* (pp. 237–252), American Geophysical Union.

Keller, E. A. (1971). Areal Sorting of Bed-load Material: The Hypothesis of Velocity Reversal. *Bulletin of the Geological Society of America*, *82*(3), 753–756.

Kieffer, S. W. (1989). Geologic Nozzles. *Reviews of Geophysics,* 27, 3–38.

Kirkby, M. J. (1986). A Two-dimensional Simulation Model for Slope and Stream Evolution, in Hillslope Processes, edited by A.D. Abrahams, Allen and Unwin, London, pp. 203–222.

Lai, Y. G., Greimann, B. P., and Wu, K. (2011). Soft Bedrock Erosion Modeling with a Two-dimensional Depth-averaged Model. *Journal of Hydraulic Engineering*, *137*(8), 804-814.

Lamb, M. P., Dietrich, W. E., and Sklar, L. S. (2008). A Model for Fluvial Bedrock Incision by Impacting Suspended and Bed Load Sediment. *Journal of Geophysical Research, 113*(F03025).

Lamb, M. P., Finnegan, N. J., Scheingross, J. S., and Sklar, L. S. (2015). New Insights into the Mechanics of Fluvial Bedrock Erosion through Flume Experiments and Theory. *Geomorphology*, *244*, 33–55.

Larsen, I. J. and Lamb, M. P. (2016). Progressive Incision of the Channeled Scablands by Outburst Floods. *Nature,* 538, 229–232.

Leutheusser, H. J., and Birk, W. M. (1991). Drownproofing of Low Overflow Structures. *Journal of Hydraulic Engineering*, *117*(2), 205–213.

MacVicar, B., and Best, J. (2013). A Flume Experiment on the Effect of Channel Width on the Perturbation and Recovery of Flow in Straight Pools and Riffles with Smooth Boundaries. *Journal of Geophysical Research: Earth Surface*, *118*(3), 1850–1863, doi: 10.1002/jgrf.20133.

MacVicar, B. J., and Rennie, C. D. (2012). Flow and Turbulence Redistribution in a Straight Artificial Pool. *Water Resources Research*, *48*(2), 1–15.

MacVicar, B. J., Obach, L., & Best, J. (2013). Large-scale Coherent Flow Structures in Alluvial Pools. *Coherent Flow Structures at Earth's Surface, First edition. Edited by Jeremy G. Venditti, James L. Best, Michael Church, and Richard J. Hardy. Published by John Wiley and Sons*, 243–259.

MacWilliams, M. L., Wheaton, J. M., Pasternack, G. B., Street, R. L., and Kitanidis, P. K. (2006). Flow Convergence Routing Hypothesis for Pool-riffle Maintenance in Alluvial Rivers. *Water Resources Research*, *42*(10), 1–21.

Murphy, B. P. Johnson, J. P. L., Gasparini, N. M., and Sklar, L. S. (2016). Chemical Weathering as a Mechanism for the Climatic Control of Bedrock River Incision. *Nature*, 532, 223–227. doi:10.1038/nature17449.

Nelson, P. A., and Seminara, G. (2011). Modeling the Evolution of Bedrock Channel Shape with Erosion from Saltating Bed Load. *Geophysical Research Letters, 38*(L17406).

Richardson, K., and Carling, P. A. (2005). A Typology of Sculpted Forms in Open Bedrock Channels. *Geological Society of America Special Paper*, *392*, 1–108.

Sawyer, A. M., Pasternack, G. B., Moir, H. J., and Fulton, A. A. (2010). Riffle-pool Maintenance and Flow Convergence Routing Observed on a Large Gravel-bed River, *Geomorphology*, 114(3), 143–160.

Scheingross, J. S., Brun, F., Lo, D. Y., Omerdin, K., and Lamb, M. P. (2014). Experimental Evidence for Fluvial Bedrock Incision by Suspended and Bedload Sediment. *Geology*, *42*(6), 523–526.

Sklar, L. S., and Dietrich, W. E. (2004). A Mechanistic Model for River Incision into Bedrock by Saltating Bed Load. *Water Resources Research, 40*(W06301).

Smits, A. J., and Wood, D. H. (1985). The Response of Turbulent Boundary Layers to Sudden Perturbations, *Annual Reviews of Fluid Mechanics*, 17, 321–358.

Sofia, G., Tarolli, P., Cazorzi, F., and Dalla Fontana, G. (2015). Downstream Hydraulic Geometry Relationships: Gathering Reference Reach-scale Width Values from LiDAR. *Geomorphology*, 250, 236–248.

Thompson, D., and Wohl, E. E. (1998). Flume Experimentation and Simulation of Bedrock Channel Processes. In *Rivers Over Rock: Fluvial Processes in Bedrock Channels*, Washington DC American Geophysical Union Geophysical Monograph Series*,* pp. 279–296.

Thompson, D. M., Nelson, J. M., and Wohl, E. E. (1998). Interactions between Pool Geometry and Hydraulics. *Water Resources Research*, *34*(12), 3673–3681.

Thompson, D. M., Wohl, E. E., and Jarrett, R. D. (1996). A Revised Velocity Reversal and Sediment Sorting Model for a High-gradient, Pool-riffle Stream. *Physical Geography*, 17(2), 142–156.

Thompson, D. M., Wohl, E. E., and Jarrett, R. D. (1999). Velocity Reversals and Sediment Sorting in Pools and Riffles Controlled by Channel Constrictions. *Geomorphology*, 27, 229–241.

Tschantz, B. A., and Wright, K. R. (2011). Hidden Dangers and Public Safety at Low-head Dams. *The Journal of Dam Safety*, *9*(1), 8–17.

Tucker, G. E., and Bras, R. L. (1998). Hillslope Processes, Drainage Density, and Landscape Morphology. *Water Resources Research*, *34*(10), 2751–2764.

Tucker, G. E., and Slingerland, R. L. (1994). Erosional Dynamics, Flexural Isostasy, and Long-lived Escarpments: A Numerical Modeling Study. *Journal of Geophysical Research*, 99(B6), 12229–12243, doi:10.1029/94JB00320.

Tucker, G. E., and Slingerland, R. (1997). Drainage Basin Responses to Climate Change. *Water Resources Research*, *33*(8), 2031–2047.

Tucker, G. E., Lancaster, S. T., Gasparini, N. M., and Bras, R. L. (2001a). The Channel-hillslope Integrated Landscape Development Model (CHILD), in *Landscape Erosion and Evolution Modeling*, edited by R. S. Harmon and W. W. Doe, pp. 349–388, Springer, New York.

Tucker, G. E., Lancaster, S. T., Gasparini, N. M., Bras, R. L., and Rybarczyk, S. M. (2001b). An Object-oriented Framework for Distributed Hydrologic and Geomorphic Modeling using Triangulated Irregular Networks, *Computers and Geoscience*, 27, 959–973.

Venditti, J. G., Rennie, C. D., Bomhof, J., Bradley, R. W., Little, M., and Church, M. (2014). Flow in Bedrock Canyons. *Nature*, *513*(7519), 534–537.

Whipple, K. X., DiBiase, R. A., and Crosby, B. T. (2013). Bedrock Rivers. In *Treatise on Geomorphology*, (9), 550–573.

Wilkinson, S. N., Keller, R. J., and Rutherfurd, I. D. (2004). Phase-shifts in Shear Stress as an Explanation for the Maintenance of Pool-riffle Sequences, *Earth Surface Processes and Landforms*, 29(6), 737–753.

Willett, S. D. (1999). Orogeny and Orography: The Effects of Erosion on the Structure of Mountain Belts. *Journal of Geophysical Research*, *104*(B12), 28.

Willgoose, G., Bras, R. L., and Rodriguez-Iturbe, I. (1991). A Coupled Channel Network Growth and Hillslope Evolution Model: 1. Theory. *Water Resources Research*, *27*(7), 1671–1684.

Wobus, C. W., Kean, J. W., Tucker, G. E., and Anderson, R. S. (2008). Modeling the Evolution of Channel Shape; Balancing Computational Efficiency with Hydraulic Fidelity. *Journal of Geophysical Research*, *113*(F2).

Wu, S., and Rajaratnarn, N. (1996). Submerged Flow Regimes of Rectangular Sharp-crested Weirs. *Journal of Hydraulic Engineering,* ASCE, 122(7), 412–414.

Appendix A. Water surface profiles and dye profiles produced with increasing sill heights at the top of a 15° entrance slope in a 10-cm-wide channel

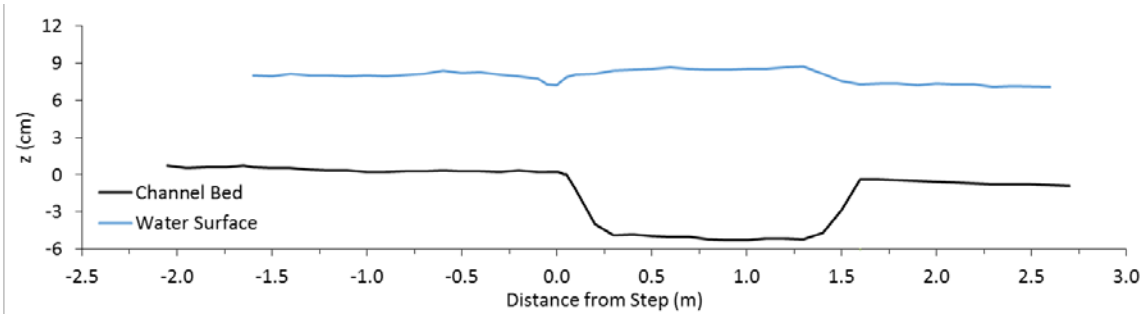

Figure A1. Water surface using no sill.

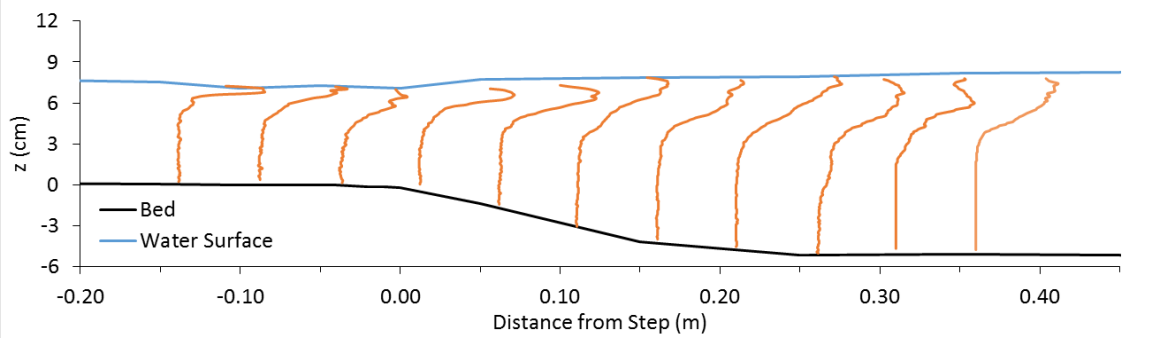

Figure A2. Dye concentration profiles using no sill.

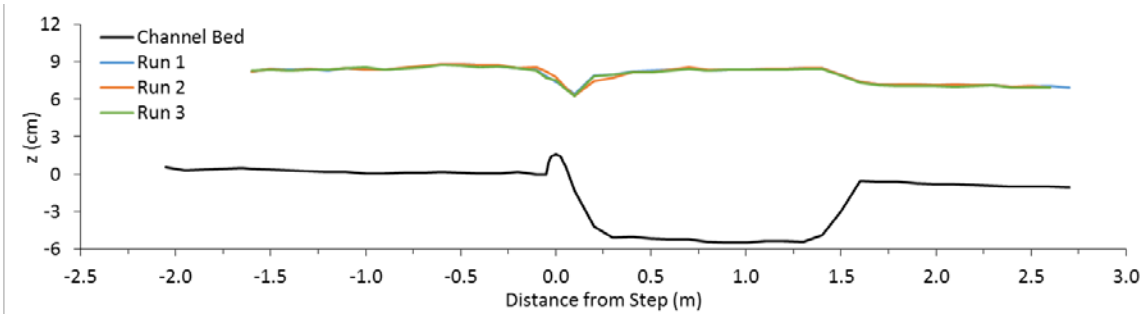

Figure A3. Water surface using 1.6 cm sill height.

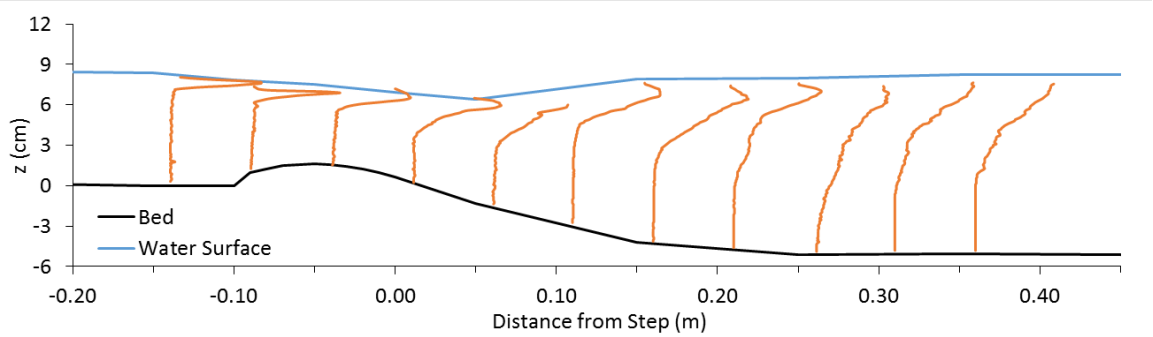

Figure A4. Dye concentration profiles using 1.6 cm sill height.

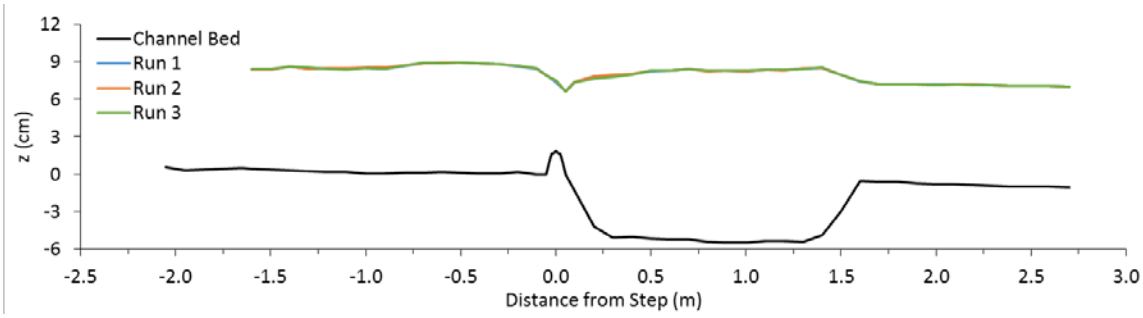

Figure A5. Water surface using 1.85 cm sill height.

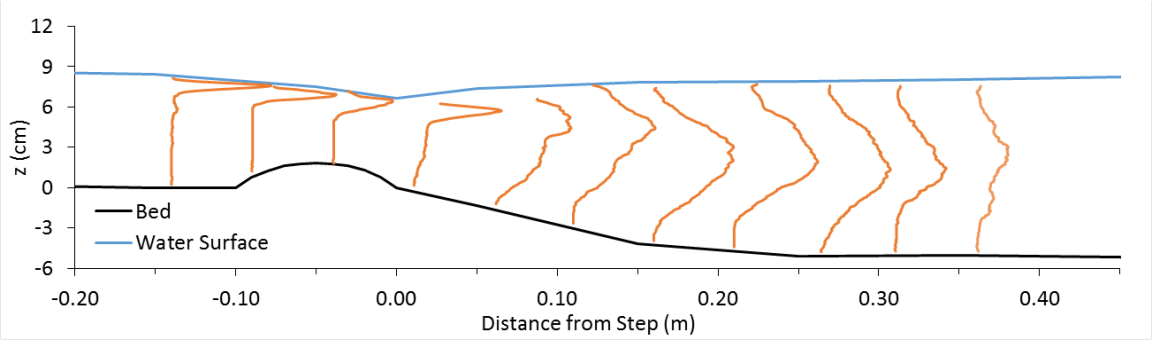

Figure A6. Dye concentration profiles using 1.85 cm sill height.

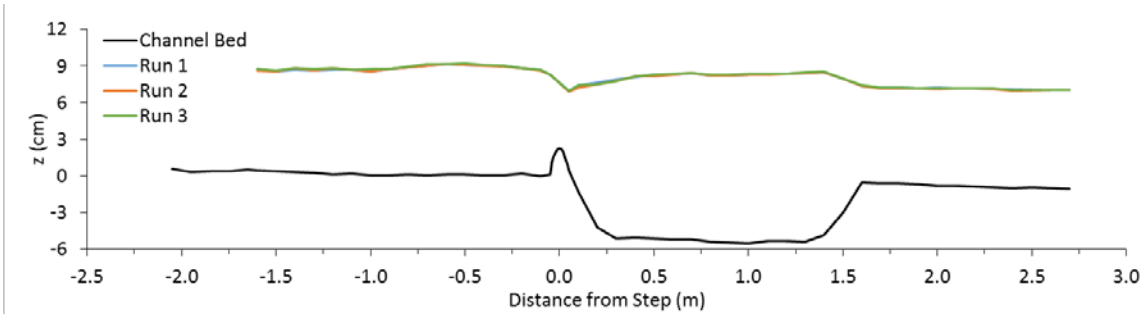

Figure A7. Water surface using 2.25 cm sill height.

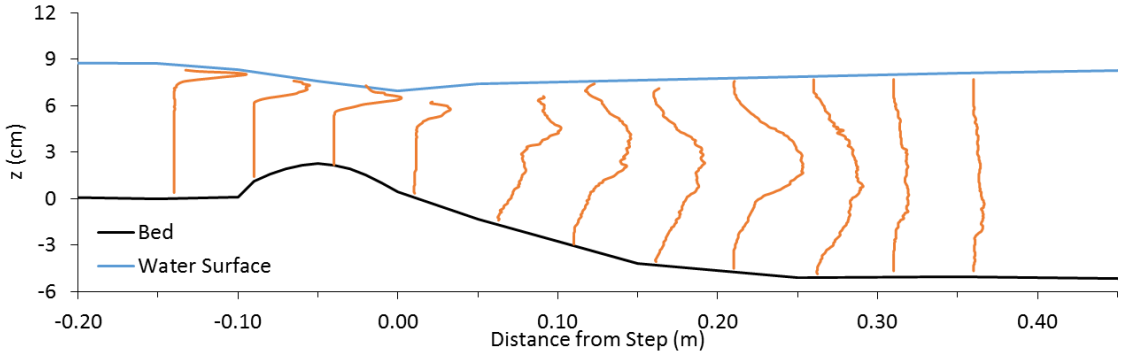

Figure A8. Dye concentration profiles using 2.25 cm sill height.

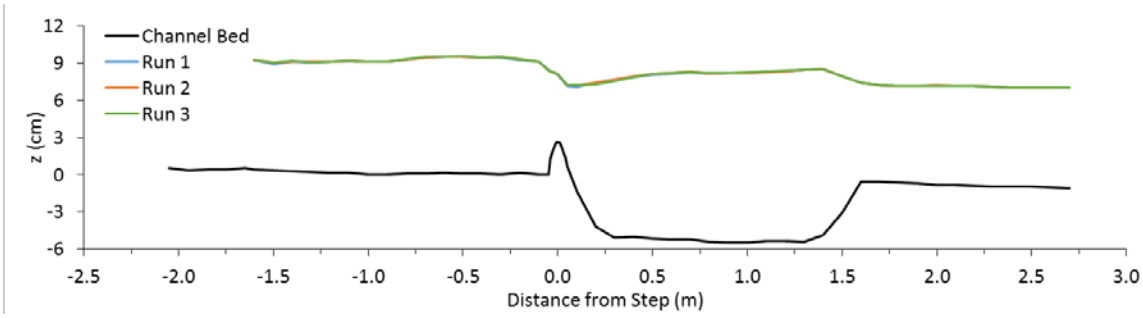

Figure A9. Water Surface using 2.65 cm sill height.

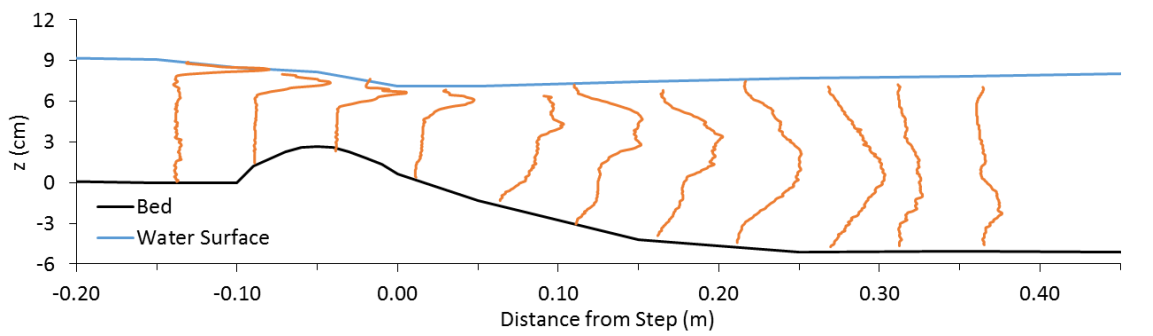

Figure A10. Dye Concentration Profiles using 2.65 cm sill height.

Appendix B. Water surface profiles and dye profiles produced with increasing channel constriction at the top of a 15° entrance slope in a 10-cm-wide channel

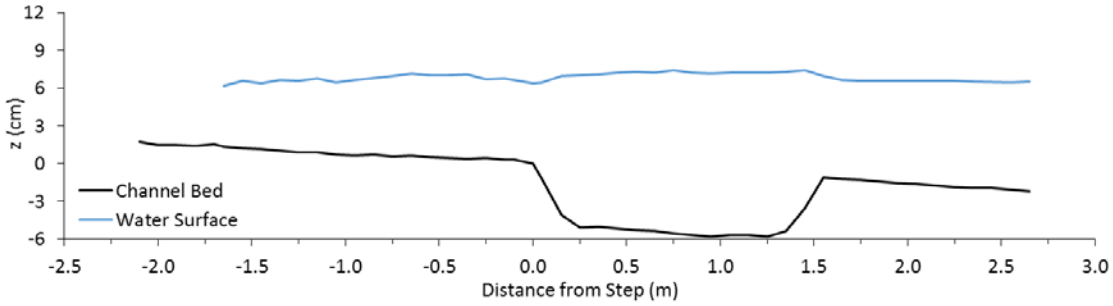

Figure B1. Water surface using no constriction.

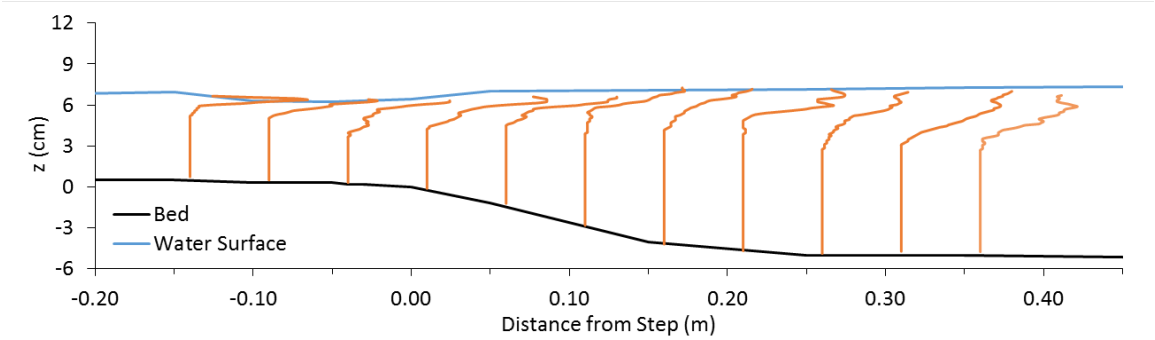

Figure B2. Dye concentration profiles using no constriction.

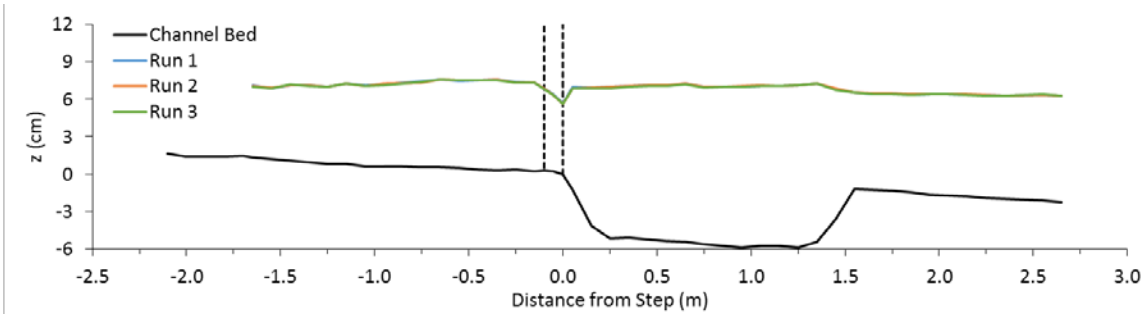

Figure B3. Water surface using 20% constriction. Location of constriction represented by dashed lines.

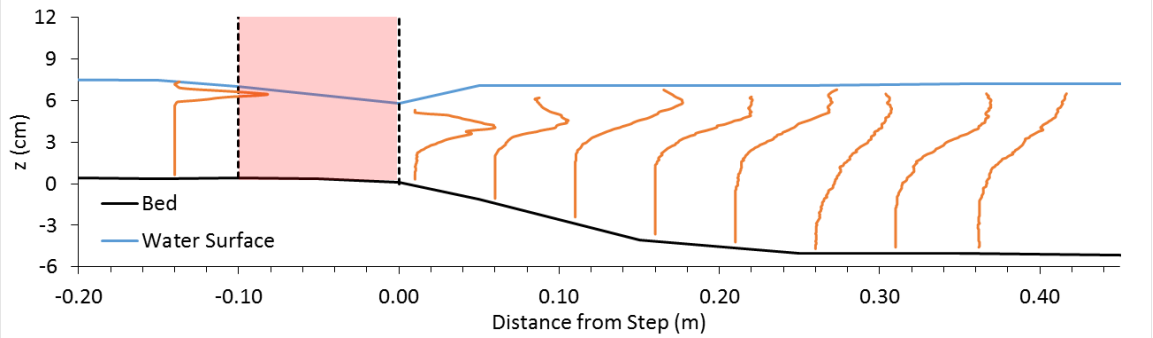

Figure B4. Dye concentration profiles using 20% constriction.

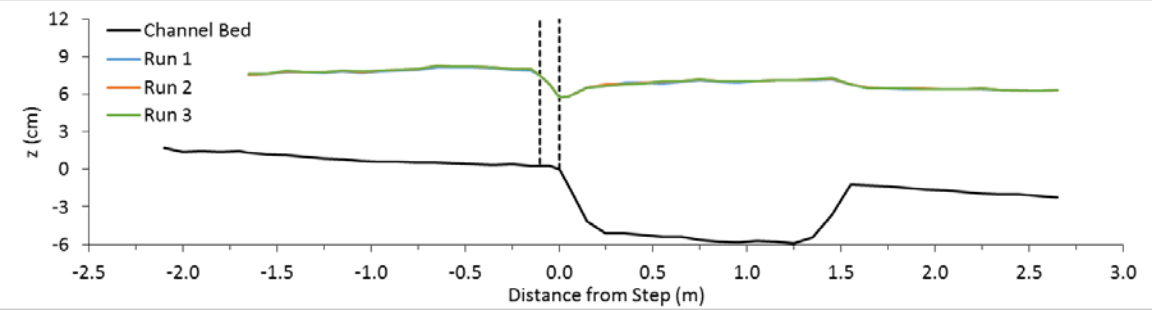

Figure B5. Water surface using 30% constriction. Location of constriction represented by dashed lines.

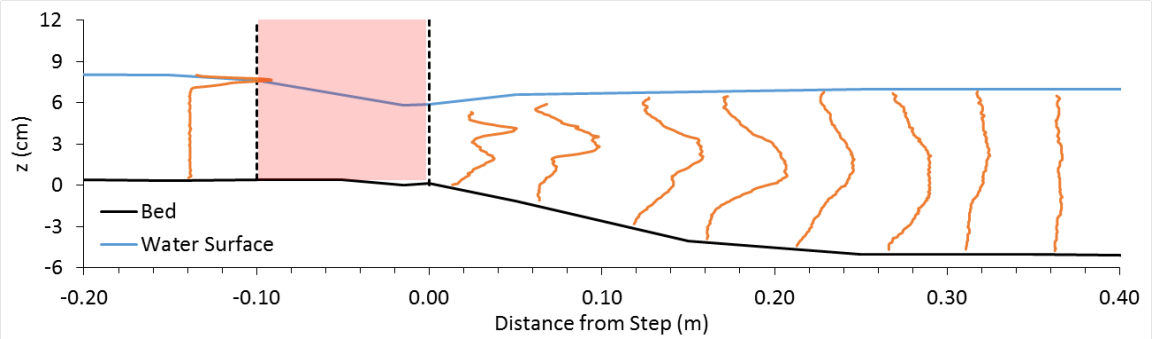

Figure B6. Dye concentration profiles using 30% constriction.

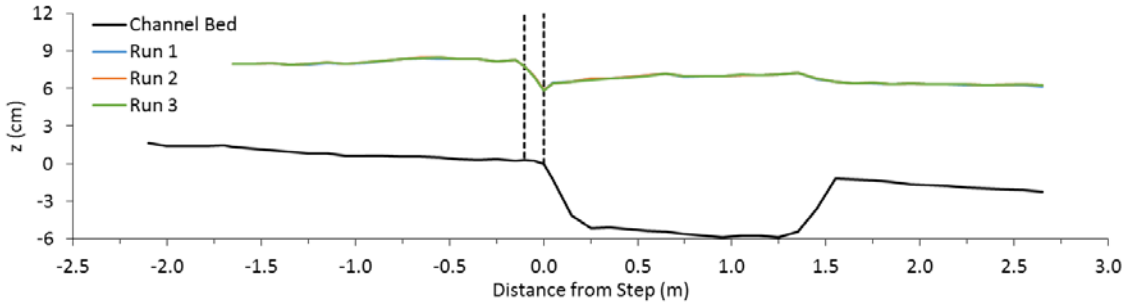

Figure B7. Water surface using 35% constriction. Location of constriction represented by dashed lines.

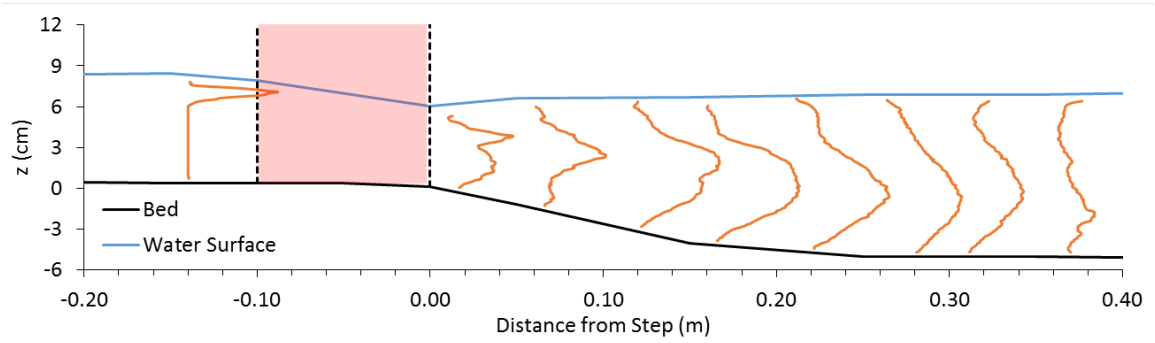

Figure B8. Dye concentration profiles using 35% constriction.

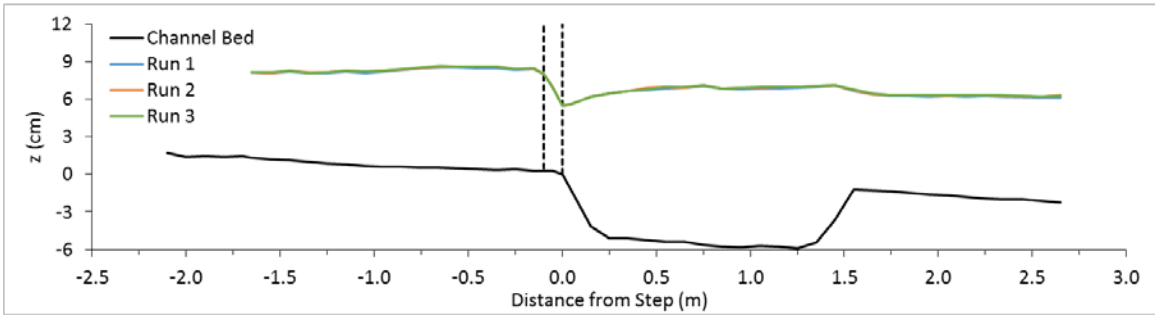

Figure B9. Water surface using 40% constriction. Location of constriction represented by dashed lines.

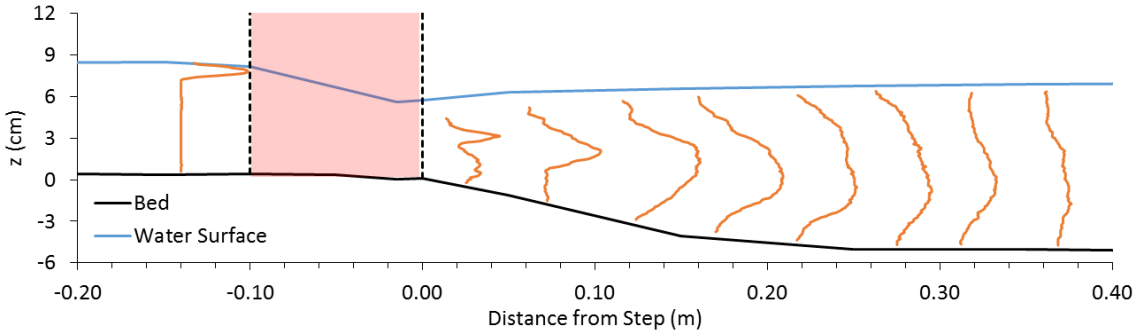

Figure B10. Dye concentration profiles using 40% constriction.

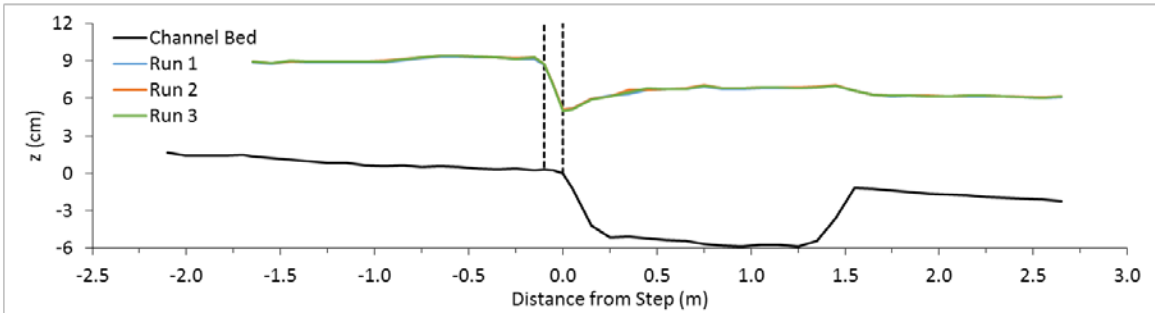

Figure B11. Water surface using 50% constriction. Location of constriction represented by dashed lines.

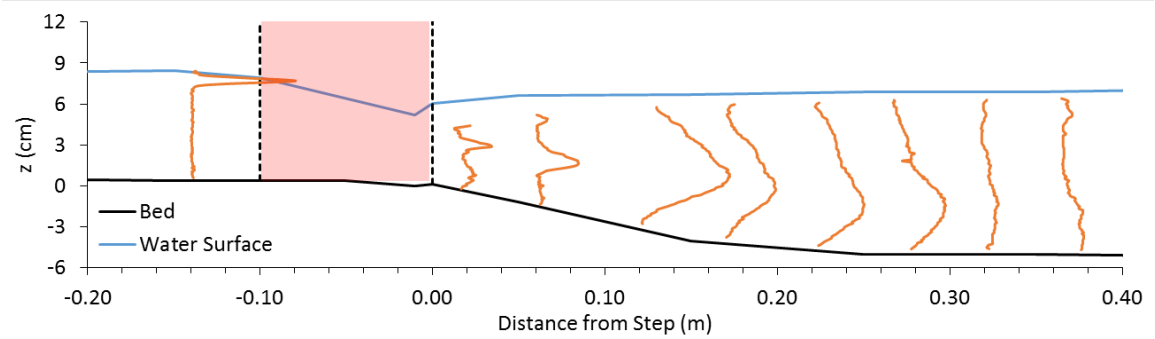

Figure B12. Dye concentration profiles using 50% constriction.

Appendix C. Water surface profiles and dye profiles produced with increasing channel constriction at the top of a 10° entrance slope in a 10-cm-wide channel

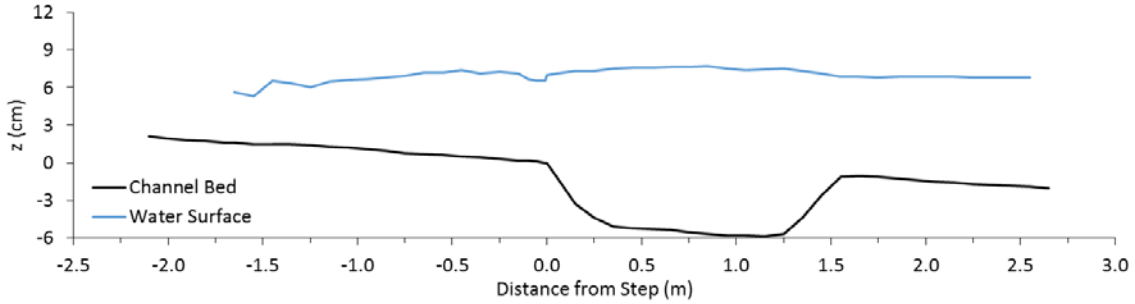

Figure C1. Water surface using no constriction.

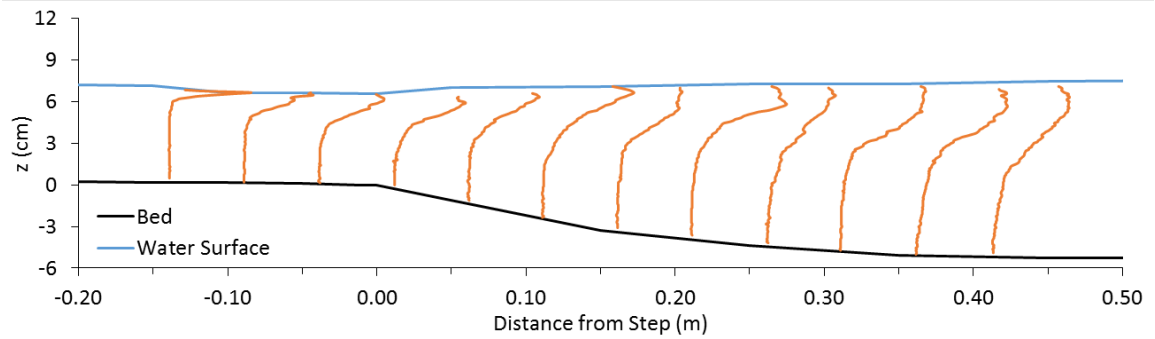

Figure C2. Dye concentration profiles using no constriction.

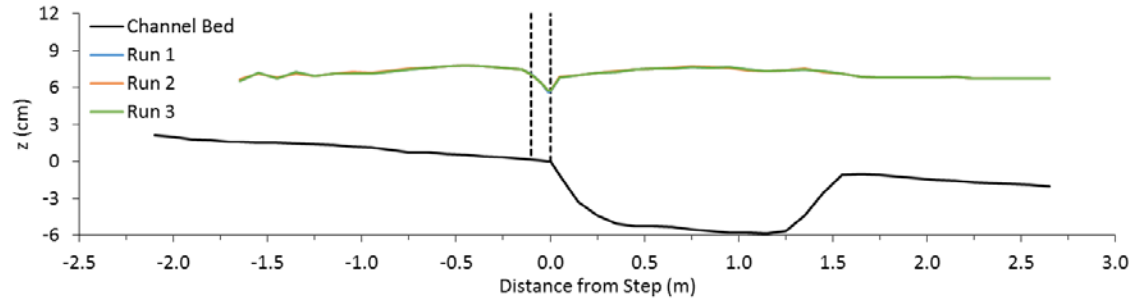

Figure C3. Water surface using 20% constriction. Location of constriction represented by dashed lines.

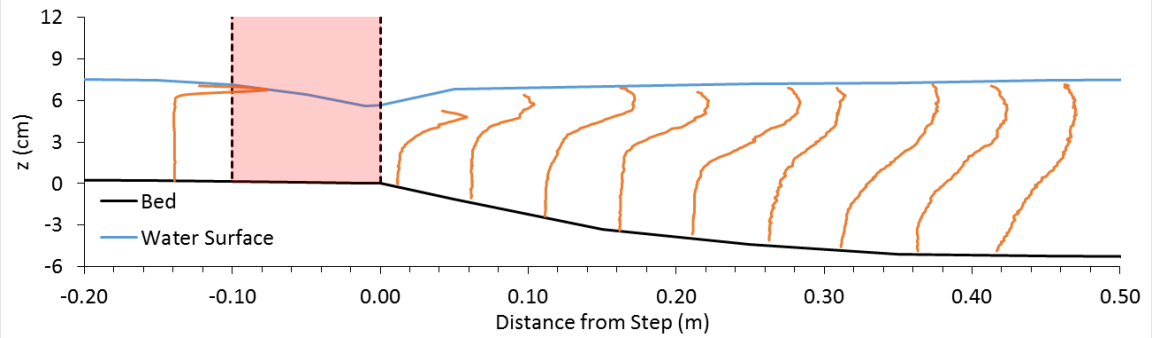

Figure C4. Dye concentration profiles using 20% constriction.

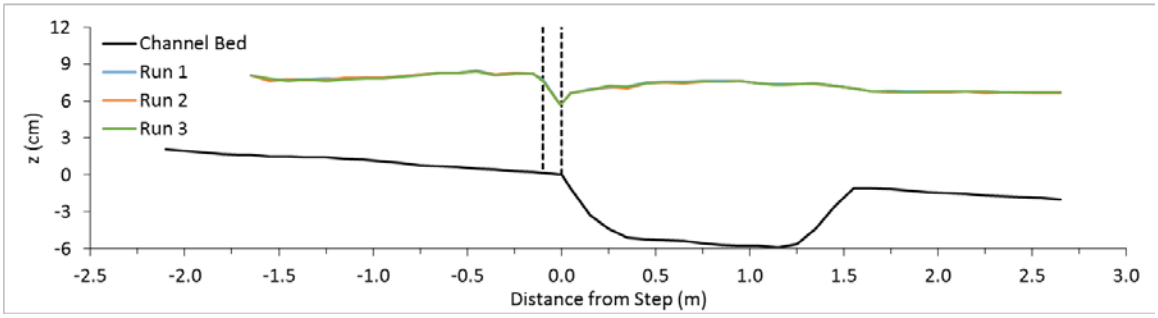

Figure C5. Water surface using 30% constriction. Location of constriction represented by dashed lines.

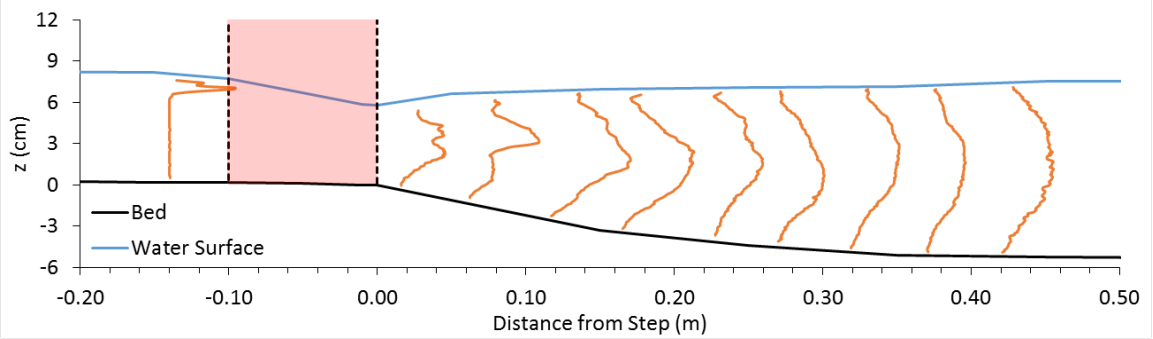

Figure C6. Dye concentration profiles using 30% constriction.

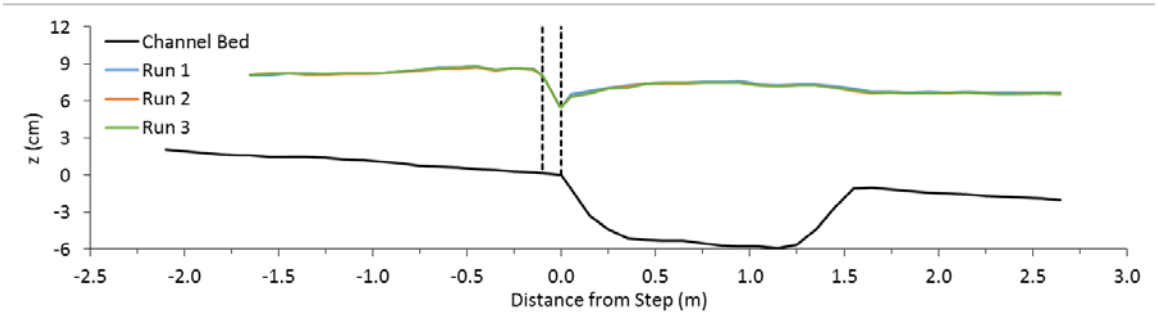

Figure C7. Water surface using 35% constriction. Location of constriction represented by dashed lines.

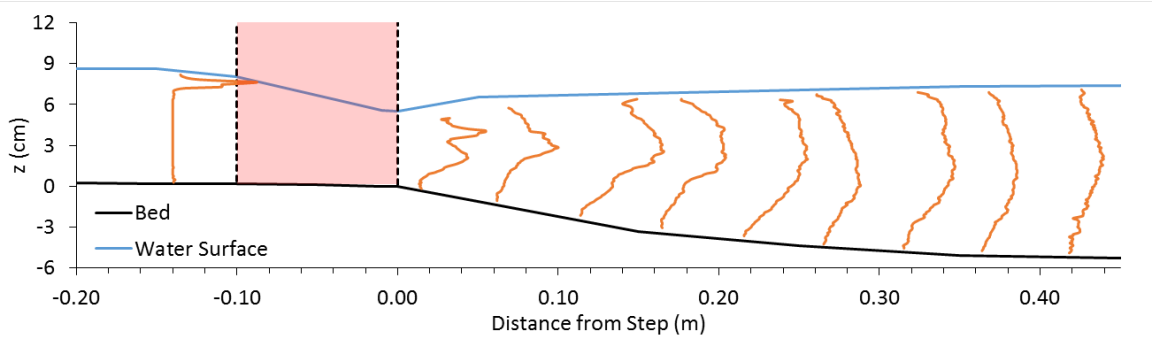

Figure C8. Dye concentration profiles using 35% constriction.

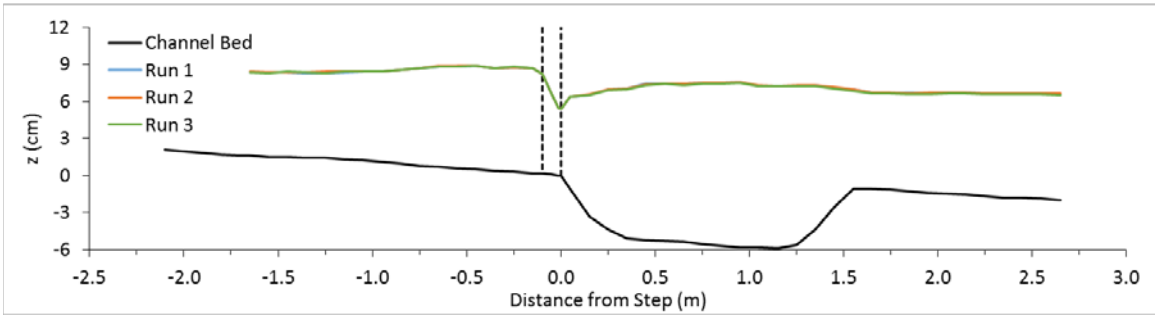

Figure C9. Water surface using 40% constriction. Location of constriction represented by dashed lines.

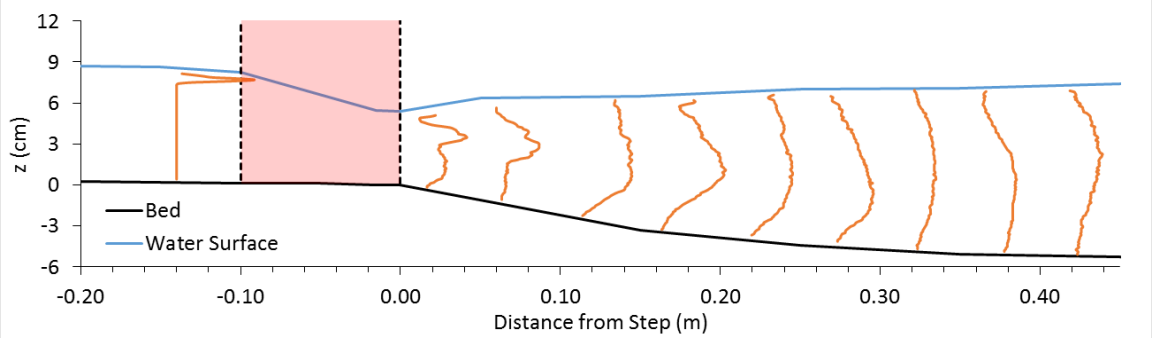

Figure C10. Dye concentration profiles using 40% constriction.

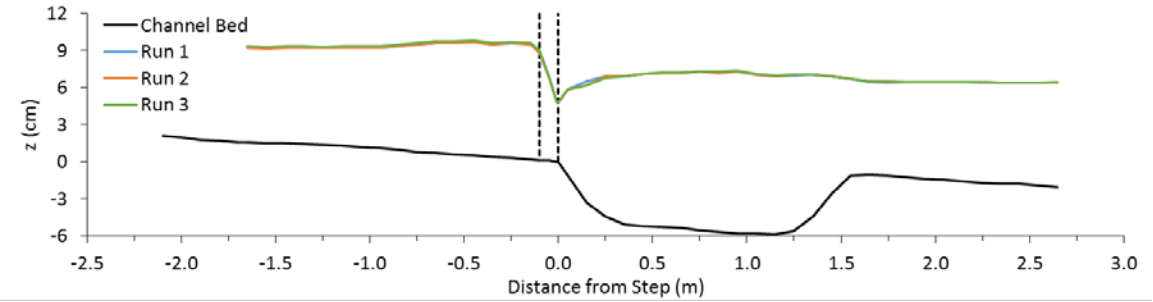

Figure C11. Water surface using 50% constriction. Location of constriction represented by dashed lines.

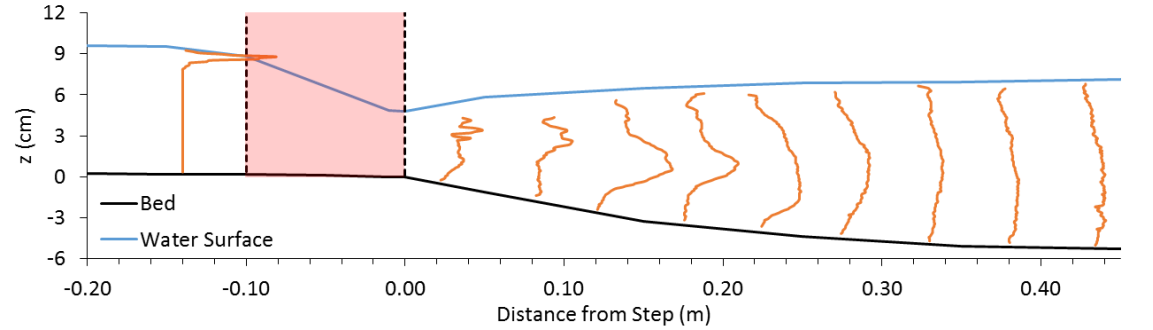

Figure C12. Dye concentration profiles using 50% constriction.

Appendix D. Water surface profiles and dye profiles produced with increasing channel constriction at the top of a 5° entrance slope in a 10-cm-wide channel

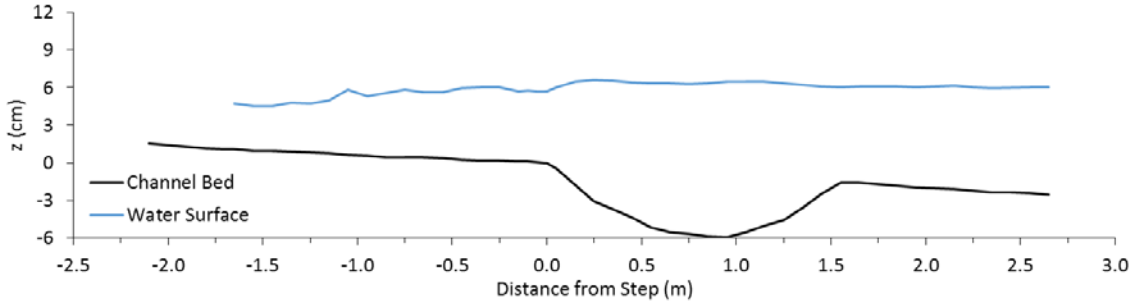

Figure D1. Water surface using no constriction.

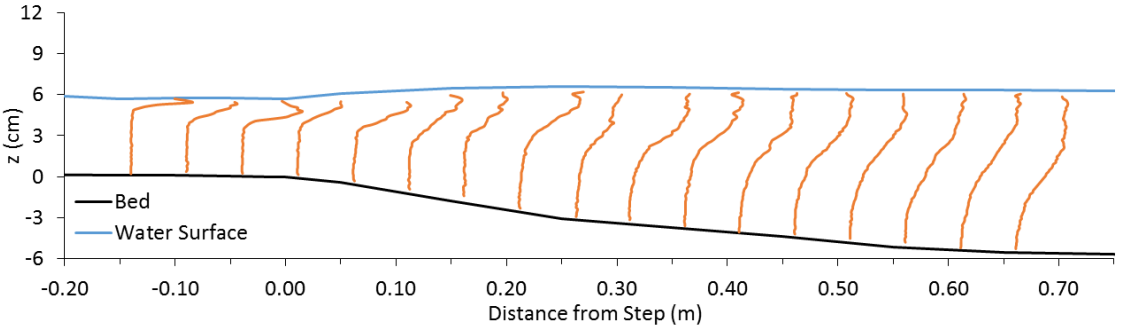

Figure D2. Dye concentration profiles using no constriction.

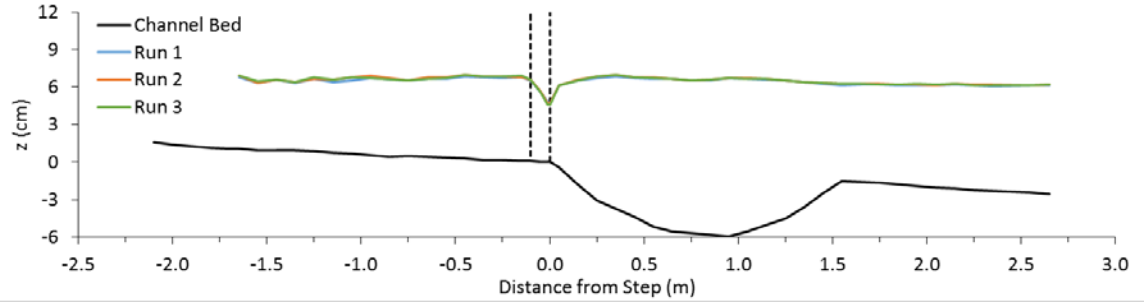

Figure D3. Water surface using 20% constriction. Location of constriction represented by dashed lines.

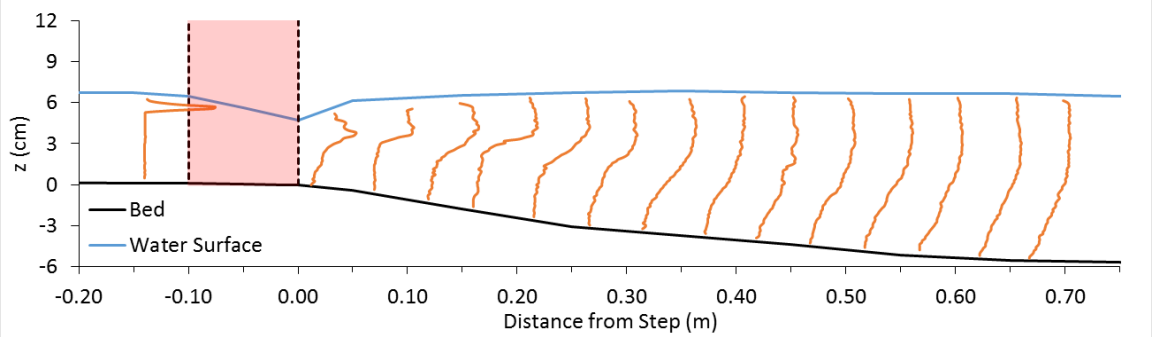

Figure D4. Dye concentration profiles using 20% constriction.

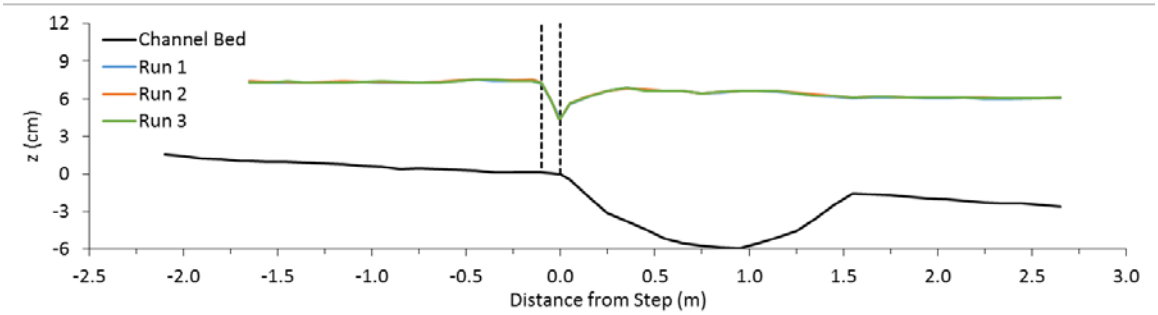

Figure D5. Water surface using 30% constriction. Location of constriction represented by dashed lines.

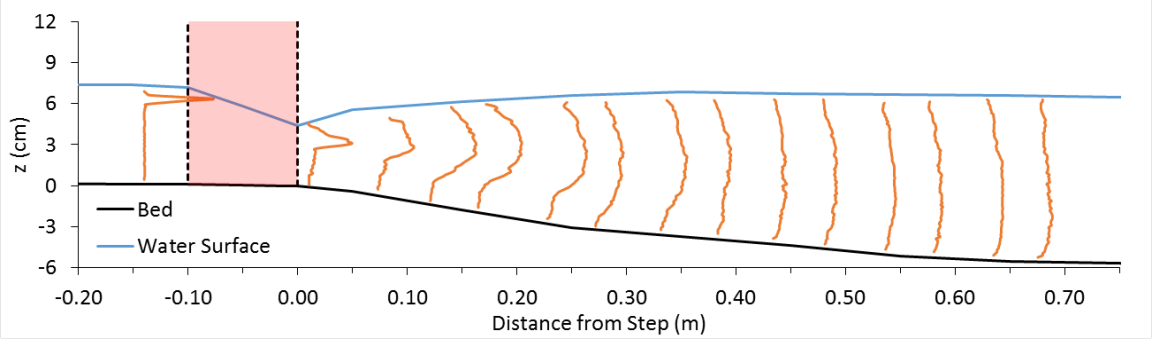

Figure D6. Dye concentration profiles using 30% constriction.

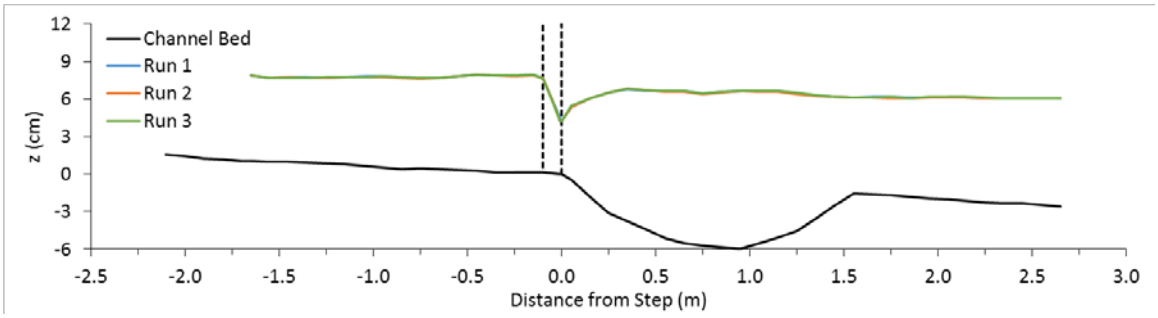

Figure D7. Water surface using 35% constriction. Location of constriction represented by dashed lines.

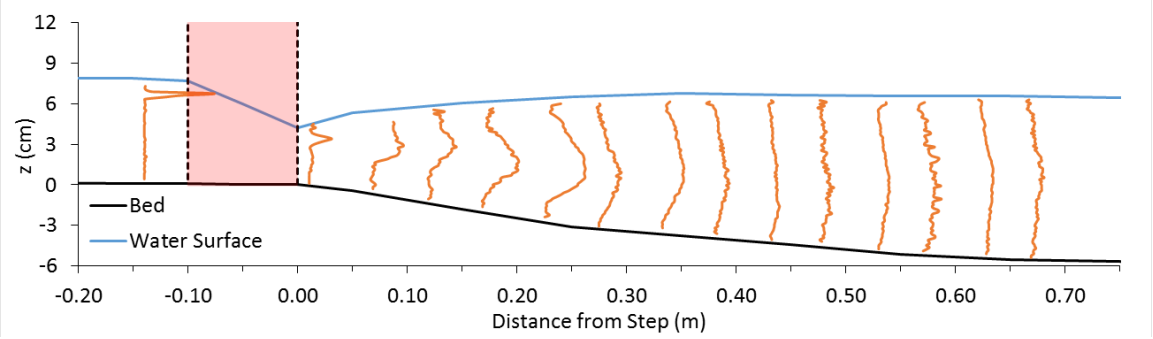

Figure D8. Dye concentration profiles using 35% constriction.

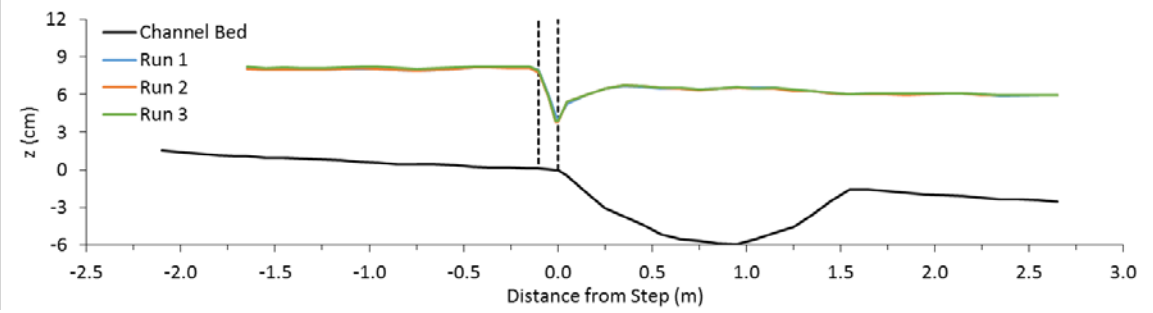

Figure D9. Water surface using 40% constriction. Location of constriction represented by dashed lines.

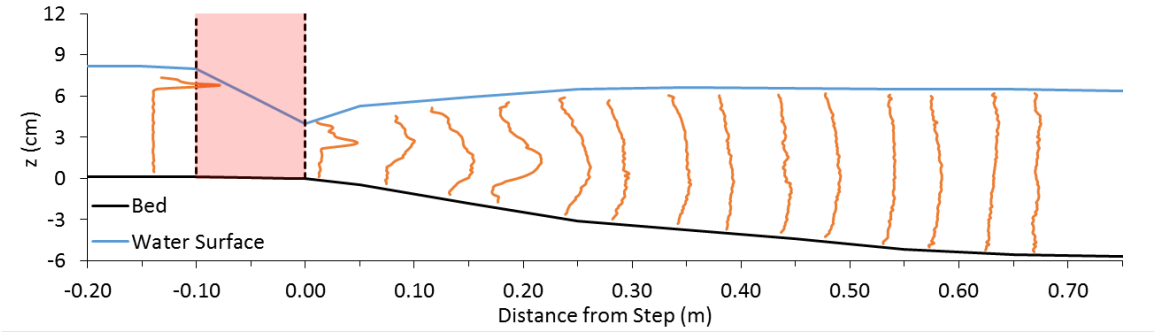

Figure D10. Dye concentration profiles using 40% constriction.

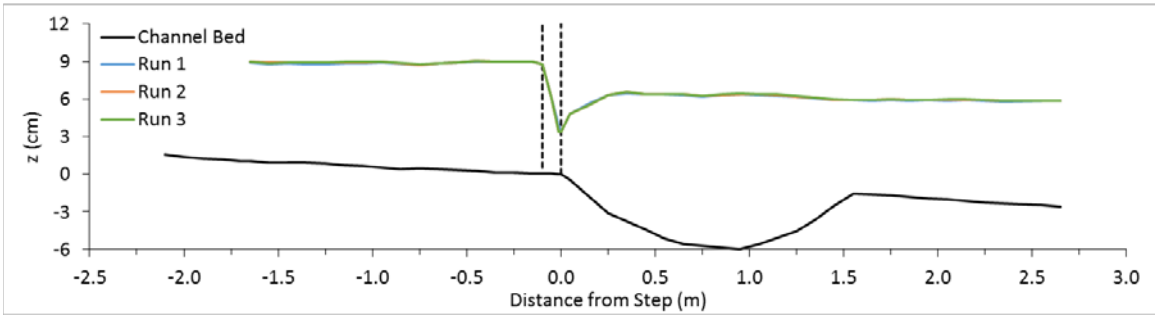

Figure D11. Water surface using 50% constriction. Location of constriction represented by dashed lines.

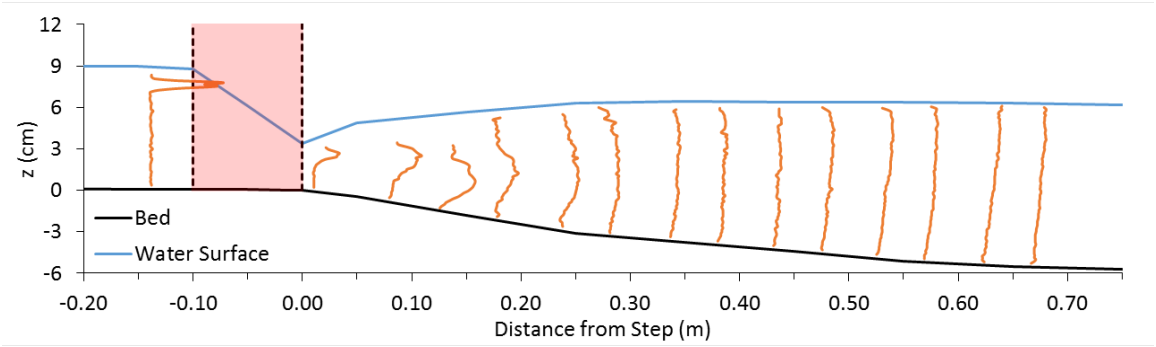

Figure D12. Dye concentration profiles using 50% constriction.

Appendix E. Water surface profiles and dye profiles produced with increasing channel constriction at the top of a 10° entrance slope using a discharge of 3 L/s in a 20-cm-wide channel

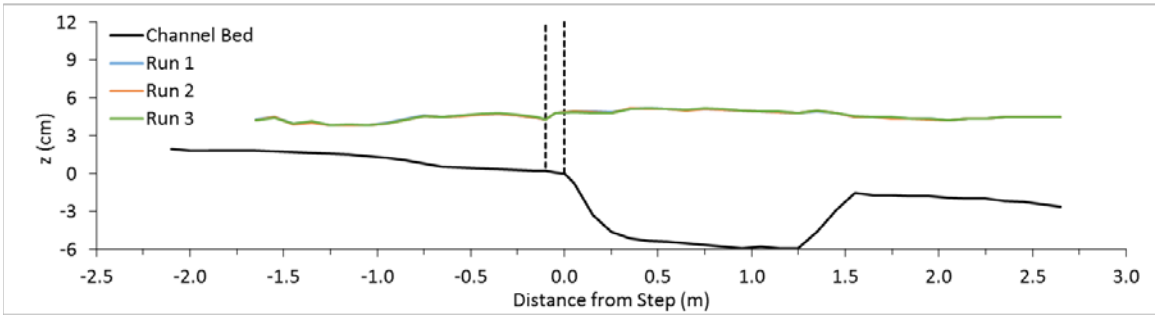

Figure E1. Water surface using no constriction.

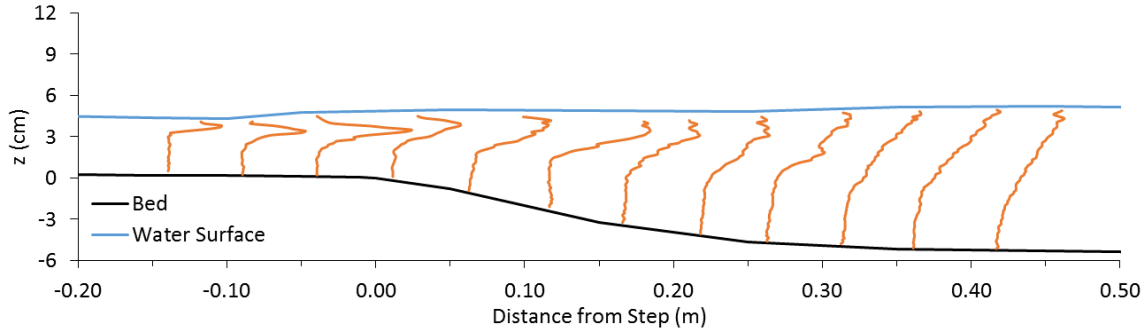

Figure E2. Dye concentration profiles using no constriction.

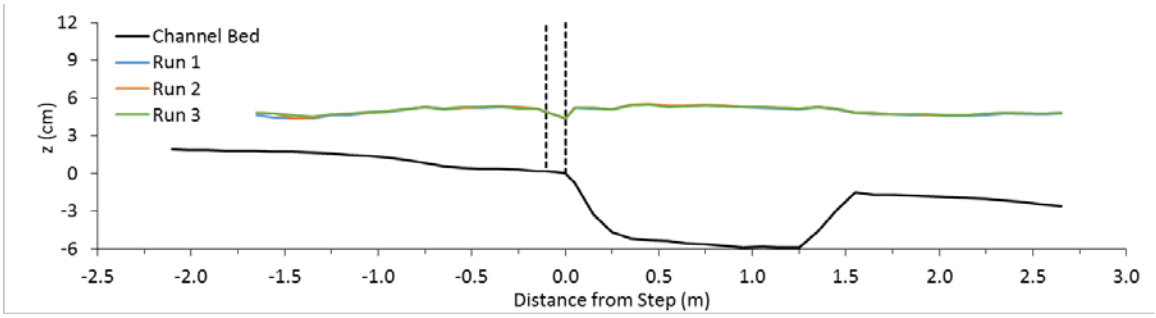

Figure E3. Water surface using 20% constriction. Location of constriction represented by dashed lines.

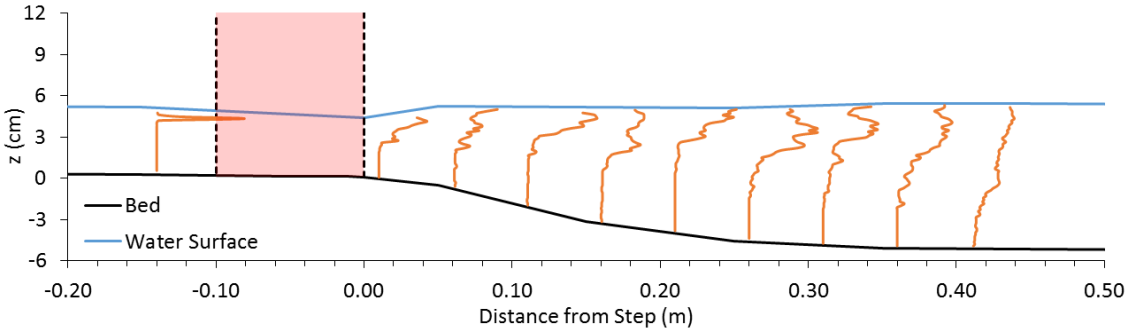

Figure E4. Dye concentration profiles using 20% constriction.

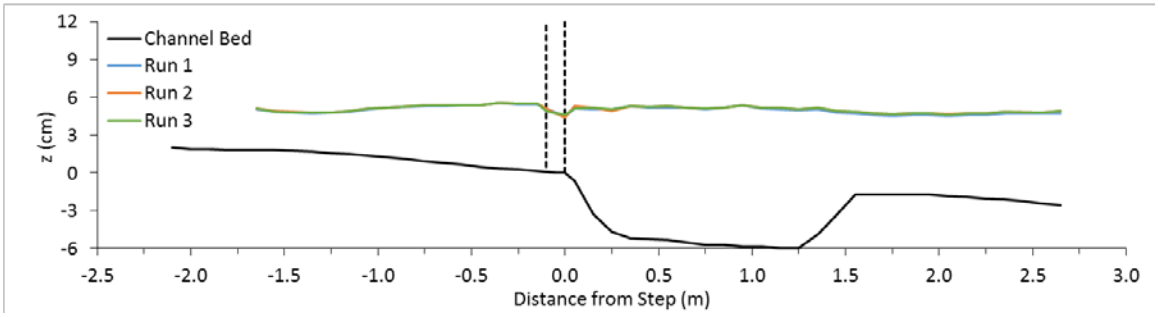

Figure E5. Water surface using 30% constriction. Location of constriction represented by dashed lines.

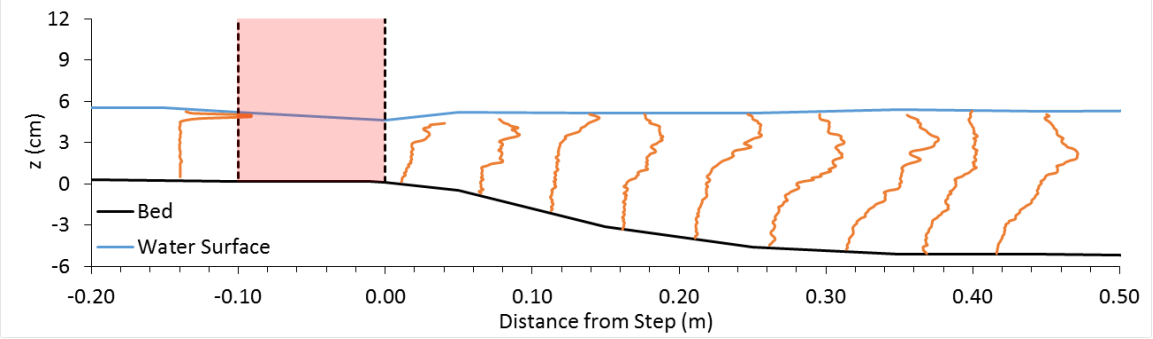

Figure E6. Dye concentration profiles using 30% constriction.

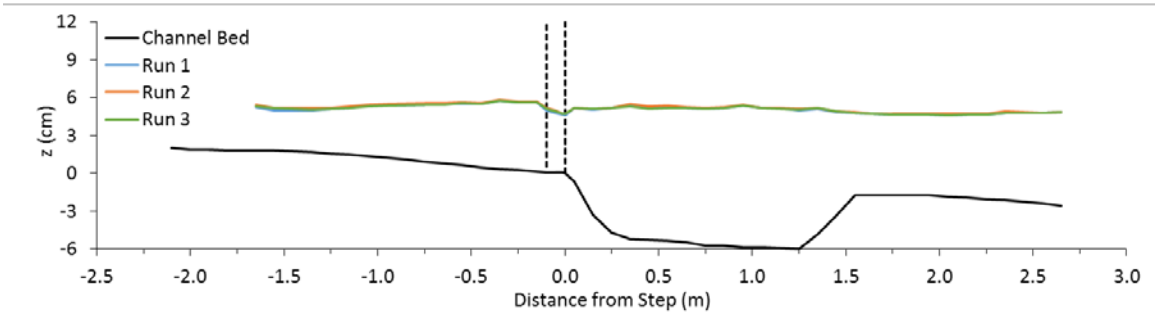

Figure E7. Water surface using 35% constriction. Location of constriction represented by dashed lines.

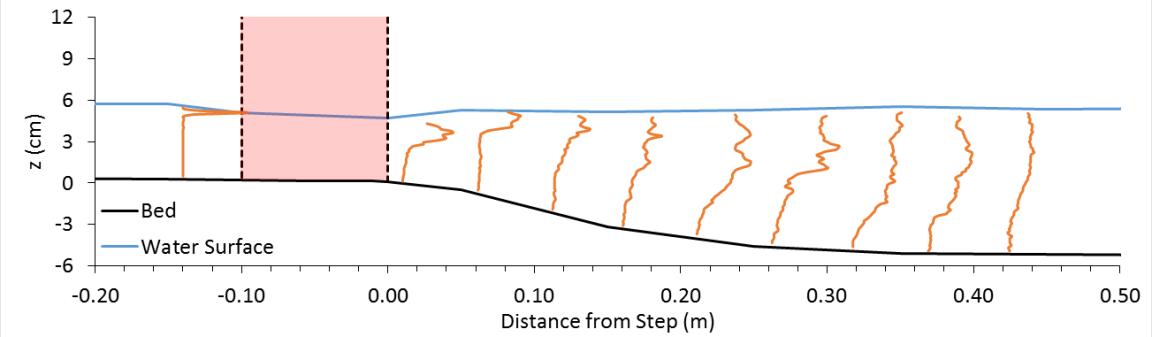

Figure E8. Dye concentration profiles using 35% constriction.

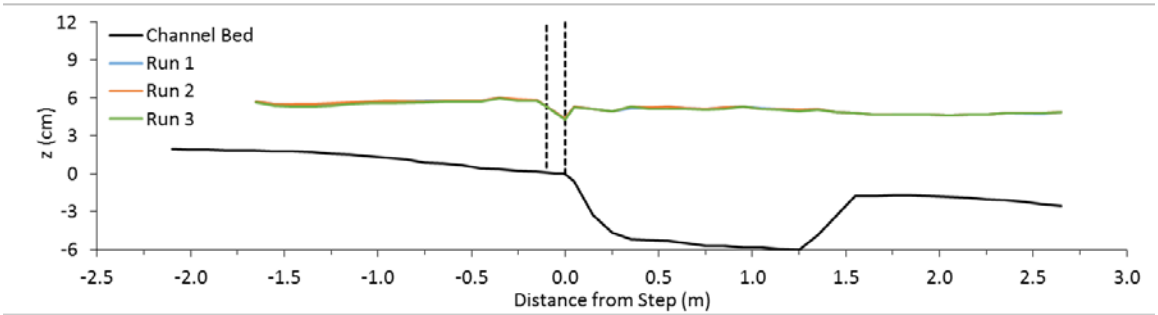

Figure E9. Water surface using 40% constriction. Location of constriction represented by dashed lines.

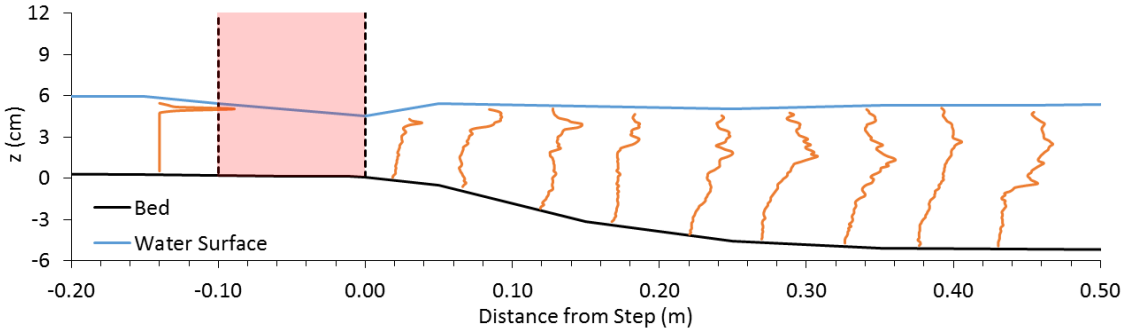

Figure E10. Dye concentration profiles using 40% constriction.

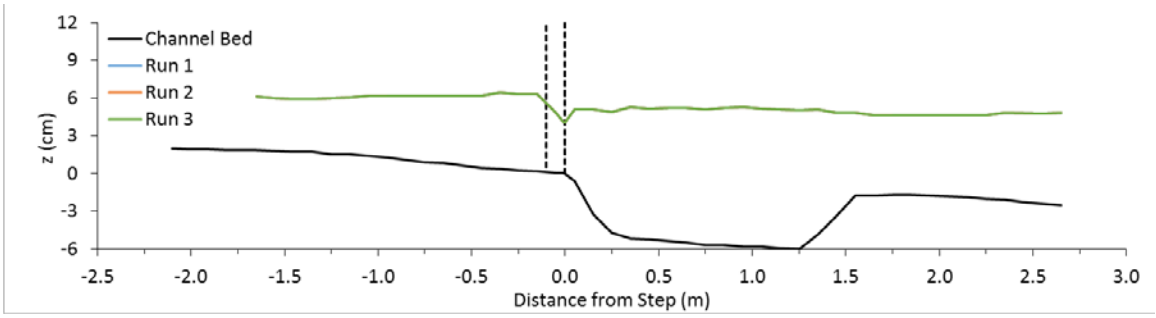

Figure E11. Water surface using 50% constriction. Location of constriction represented by dashed lines.

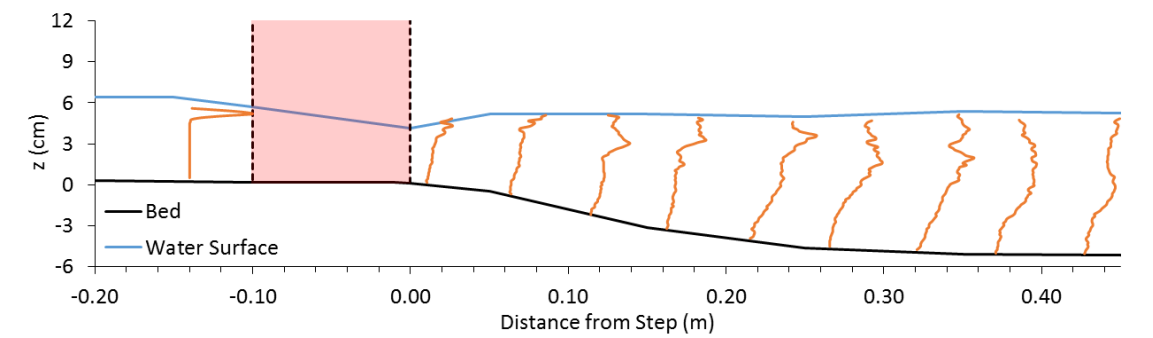

Figure E12. Dye concentration profiles using 50% constriction.

Appendix F. Water surface profiles and dye profiles produced with increasing channel constriction at the top of a 10° entrance slope using a discharge of 6 L/s in a 20-cm-wide channel

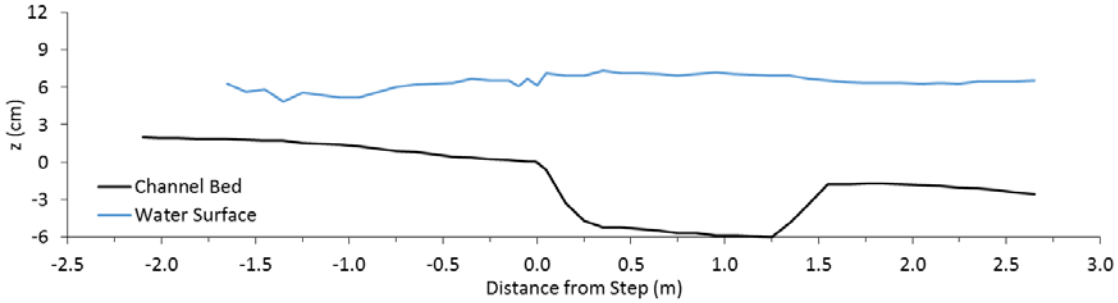

Figure F1. Water surface using no constriction.

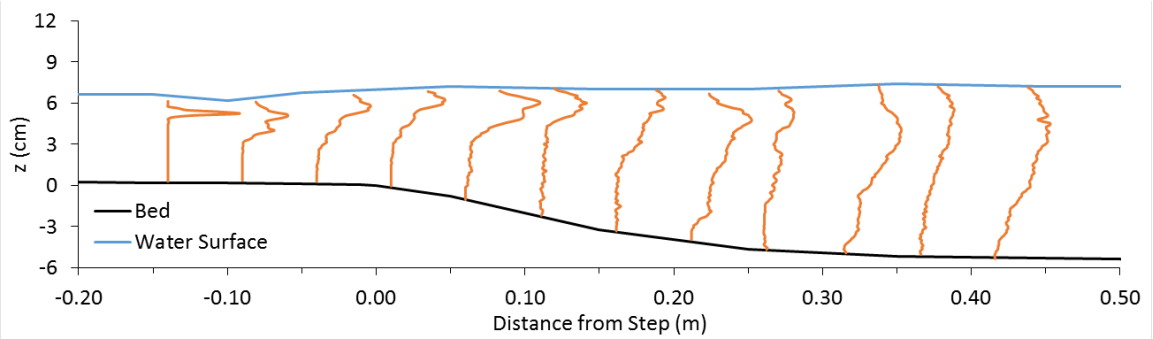

Figure F2. Dye concentration profiles using no constriction.

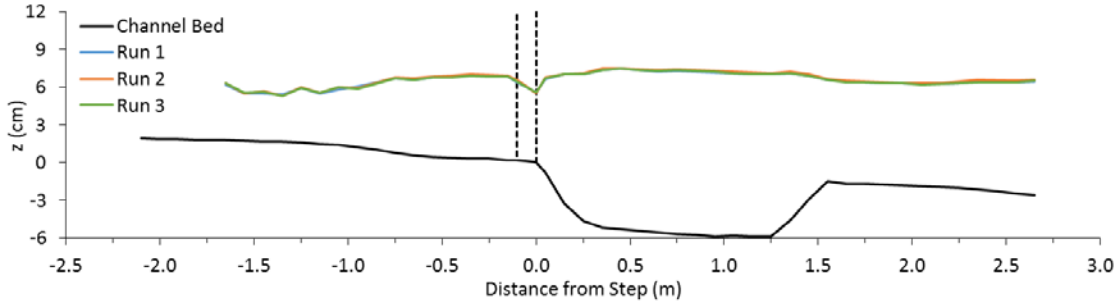

Figure F3. Water surface using 20% constriction. Location of constriction represented by dashed lines.

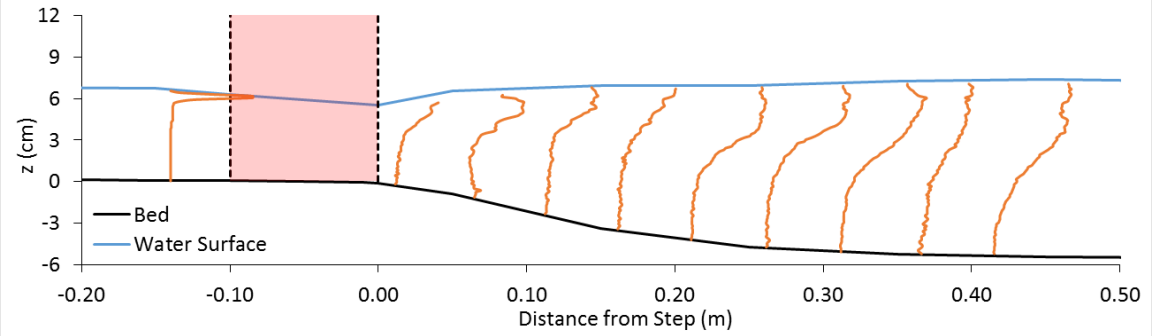

Figure F4. Dye concentration profiles using 20% constriction.

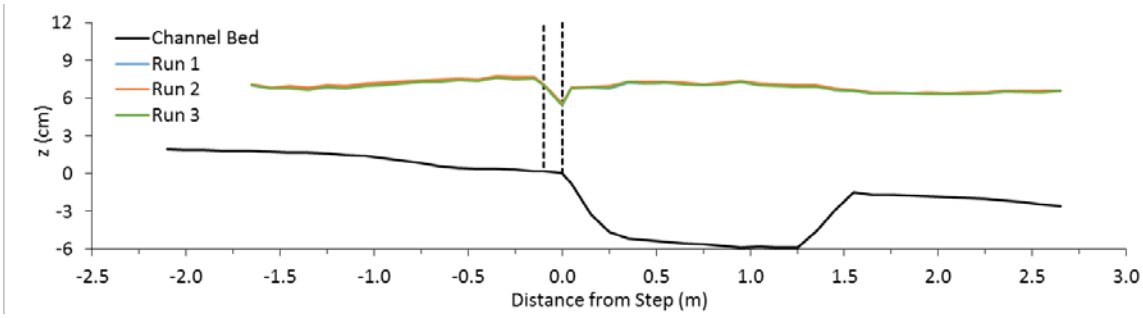

Figure F5. Water surface using 30% constriction. Location of constriction represented by dashed lines.

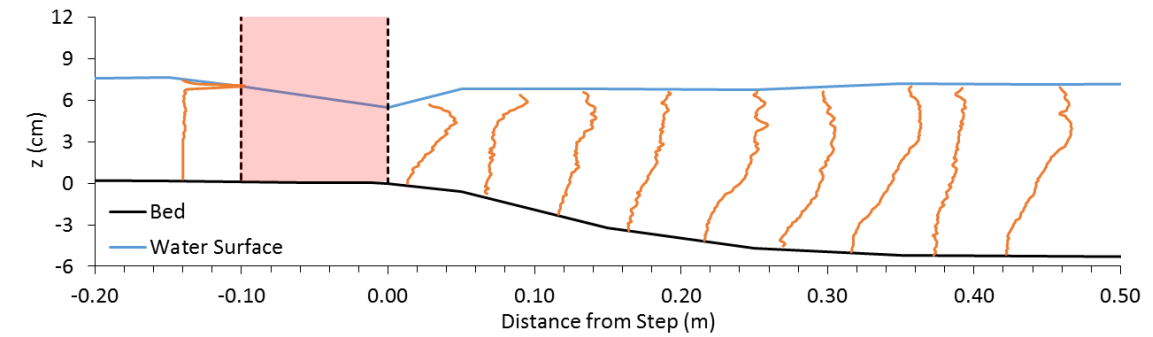

Figure F6. Dye concentration profiles using 30% constriction.

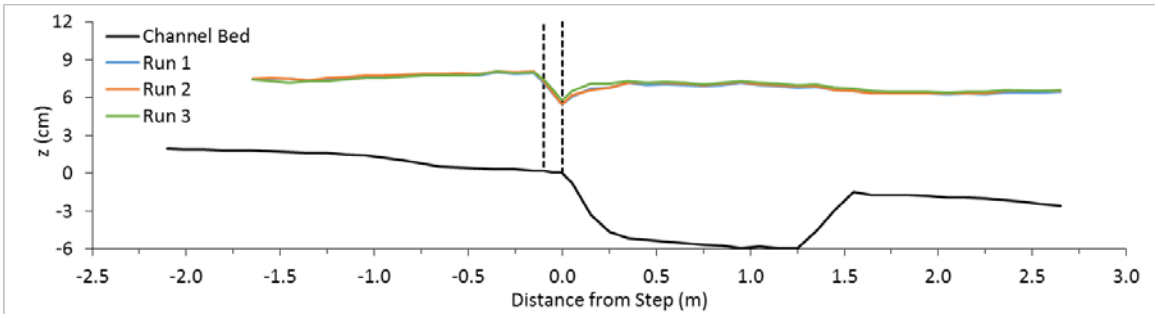

Figure F7. Water surface using 35% constriction. Location of constriction represented by dashed lines.

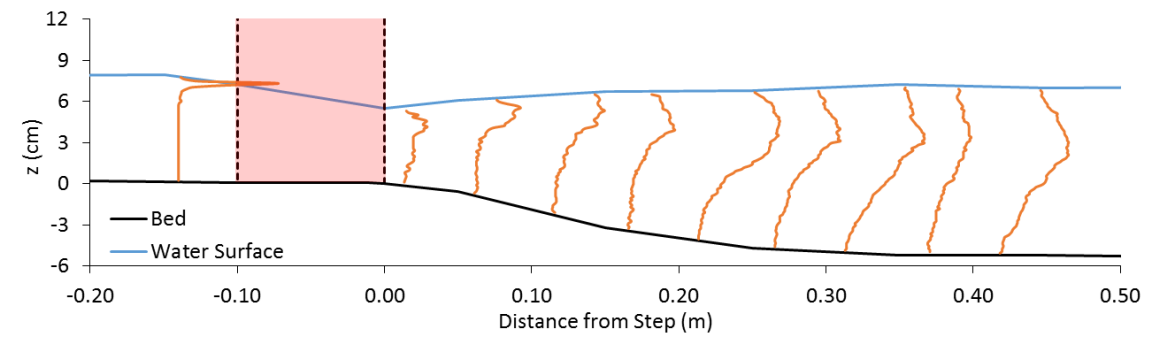

Figure F8. Dye concentration profiles using 35% constriction.

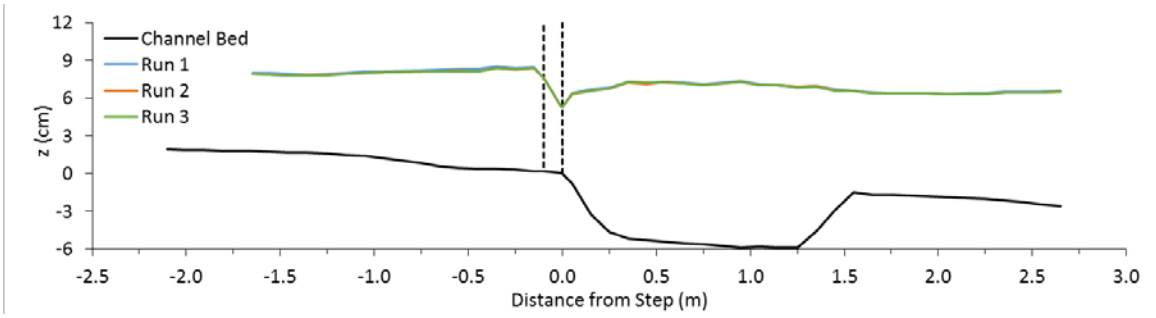

Figure F9. Water surface using 40% constriction. Location of constriction represented by dashed lines.

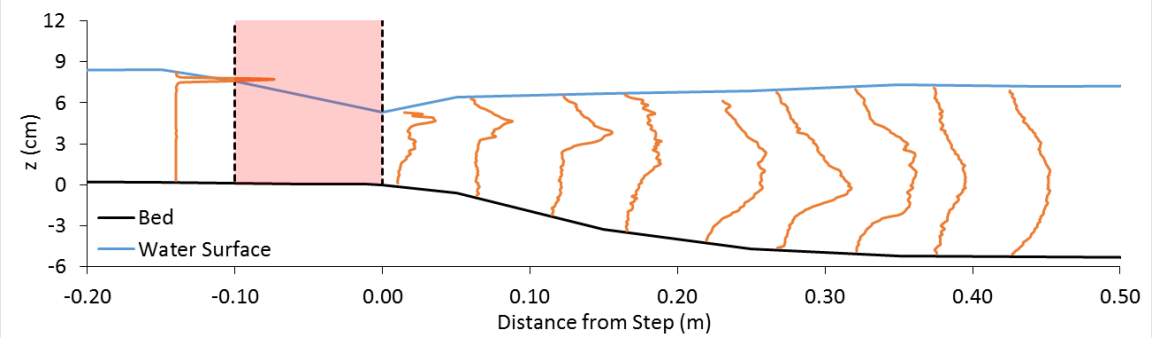

Figure F10. Dye concentration profiles using 40% constriction.

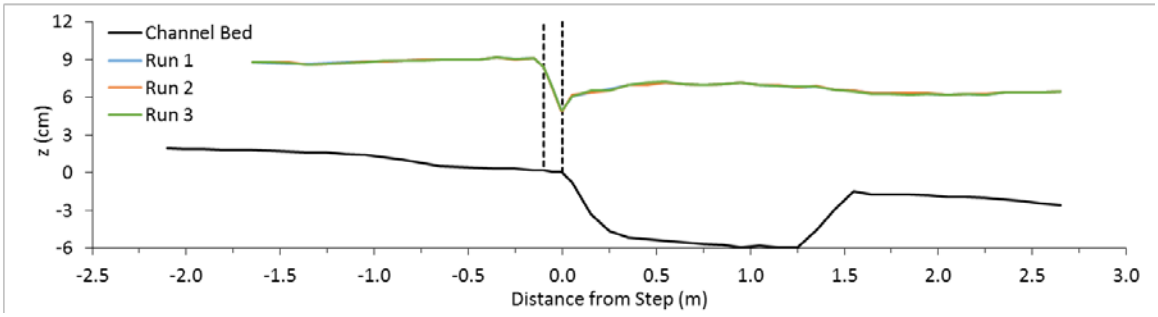

Figure F11. Water surface using 50% constriction. Location of constriction represented by dashed lines.

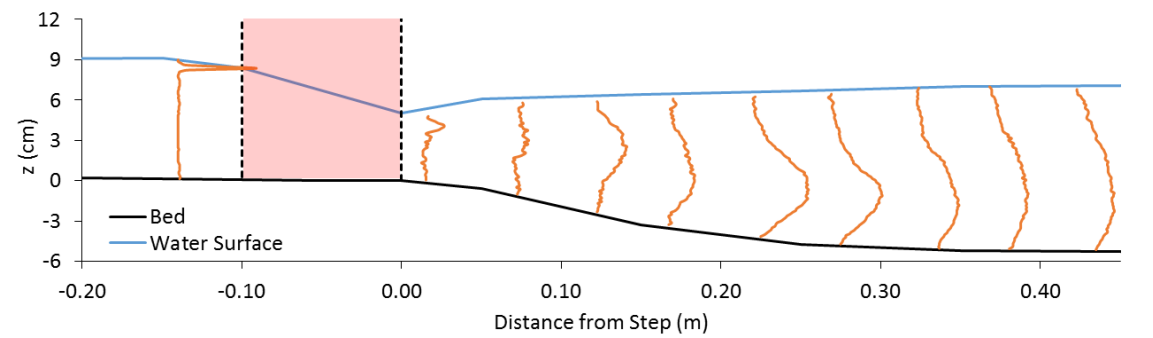

Figure F12. Dye concentration profiles using 50% constriction.

Appendix G. Water surface and dye profiles produced with increasing channel constriction at the top of a 10° entrance slope in a 20-cm-wide channel with Froude number matched to the 10-cm-wide channel

Discharge was adjusted until the Froude number at the constriction crest equaled that using the same constriction in the 10-cm-wide channel in order to compare the occurrence and strength of plunging flow while maintaining a constant Froude number at the constriction crest. These data are not presented in the article.

Table 1. Flow conditions for experiments using constant Froude number at constriction crest

Run #	Constriction width		Ent. S	w	w/d_1	Q	Depth				Velocity			Froude #			Strength
	cm	%	°	cm		L s^{-1}	d_1 cm	d_c cm	d_2 cm	d_3 cm	V_1 cm s^{-1}	V_c cm s^{-1}	V_2 cm s^{-1}	Fr_1	Fr_c	Fr_2	
C6	1.0	20	10	10	1.4	3	7.3	6.3	13.3	8.3	40	60	22	0.48	0.76	0.19	n/a
C7	1.5	30	10	10	1.3	3	8.0	6.6	13.3	8.3	37	65	22	0.42	0.81	0.19	mod.
C8	1.8	35	10	10	1.2	3	8.3	6.6	13.3	8.2	36	71	22	0.39	0.88	0.19	mod.
C9	2.0	40	10	10	1.2	3	8.4	6.5	13.2	8.2	35	77	22	0.39	0.96	0.20	strong
C10	2.5	50	10	10	1.1	3	9.3	6.7	13.0	8.0	32	90	23	0.33	1.10	0.20	strong
F1	2.0	20	10	20	3.9	4.4	5.1	4.6	11.4	6.7	42	60	19	0.60	0.89	0.18	n/a
F2	3.0	30	10	20	2.9	6.4	7.0	6.3	12.9	8.2	45	73	24	0.54	0.92	0.22	weak
F3	3.6	35	10	20	2.5	7.2	7.9	7.2	13.4	8.7	45	77	26	0.51	0.92	0.23	mod.
F4	4.0	40	10	20	2.4	7.2	8.4	7.1	13.4	8.7	42	85	26	0.46	1.01	0.23	mod.
F5	5.0	50	10	20	2.2	6.4	8.9	7.0	13.2	8.4	35	91	24	0.38	1.10	0.21	strong

V_1 and V_c correspond to d_1 and d_c. Fr_1 and Fr_c correspond to d_1 and d_c. V_2 and Fr_2 measured downstream of recirculation zone.

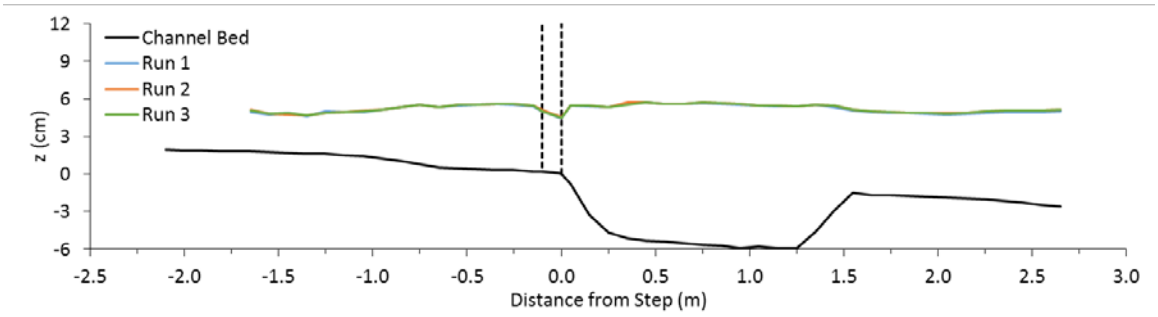

Figure G1. Fr_c = 0.89. Corresponding to Run C6. Water surface using 20% constriction. Location of constriction represented by dashed lines.

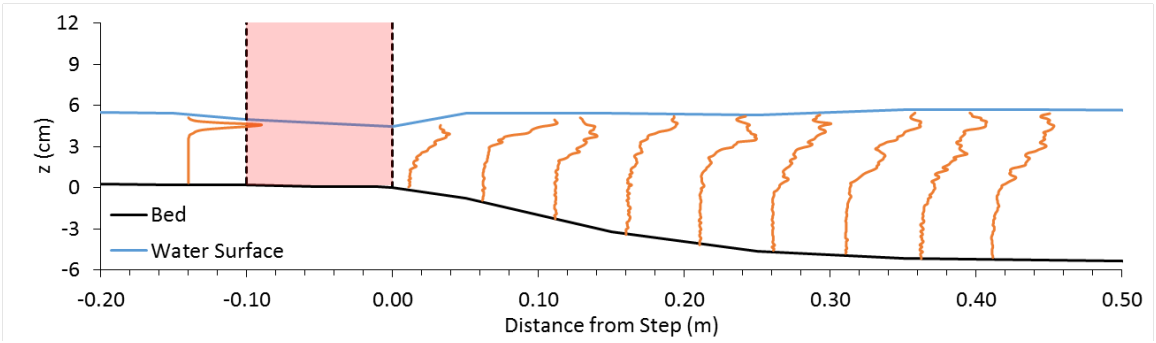

Figure G2. Fr_c = 0.89. Corresponding to Run C6. Dye concentration profiles using 20% constriction.

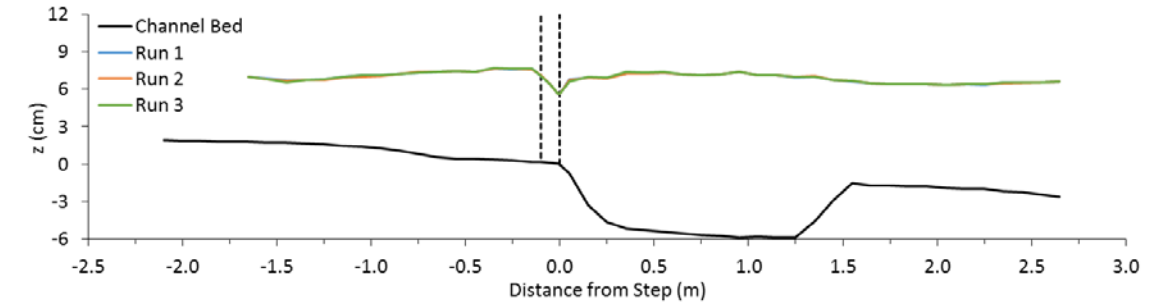

Figure G3. Fr_c = 0.92. Corresponding to Run C7. Water surface using 30% constriction. Location of constriction represented by dashed lines.

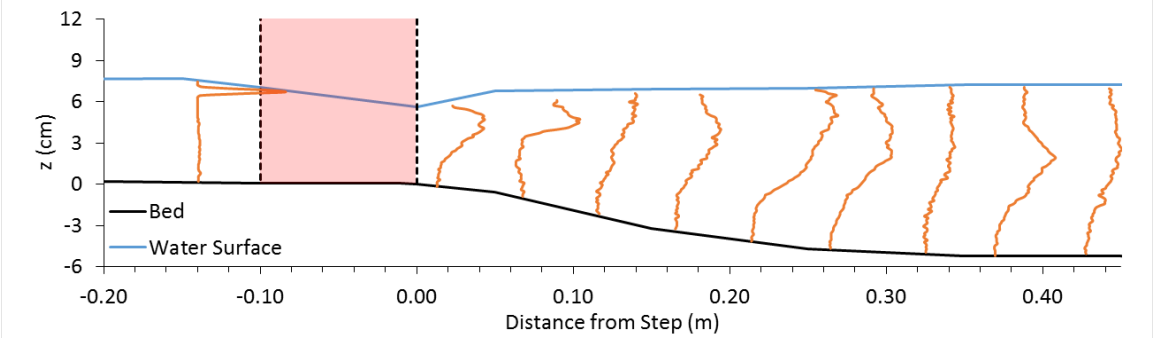

Figure G4. Fr_c = 0.92. Corresponding to Run C7. Dye concentration profiles using 30% constriction.

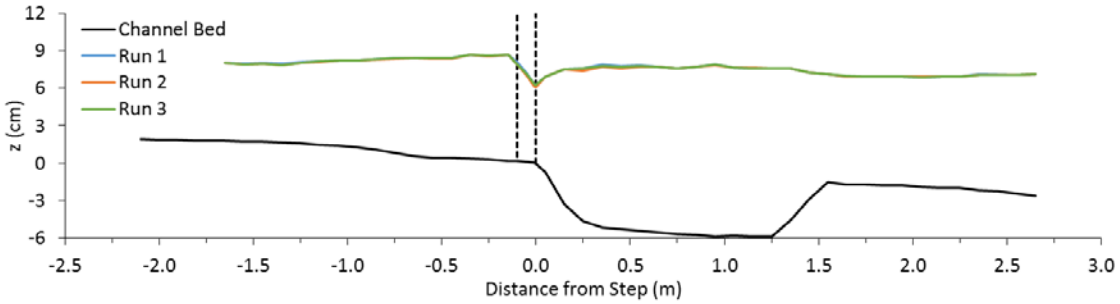

Figure G5. Fr_c = 0.92. Corresponding to Run C8. Water surface using 35% constriction. Location of constriction represented by dashed lines.

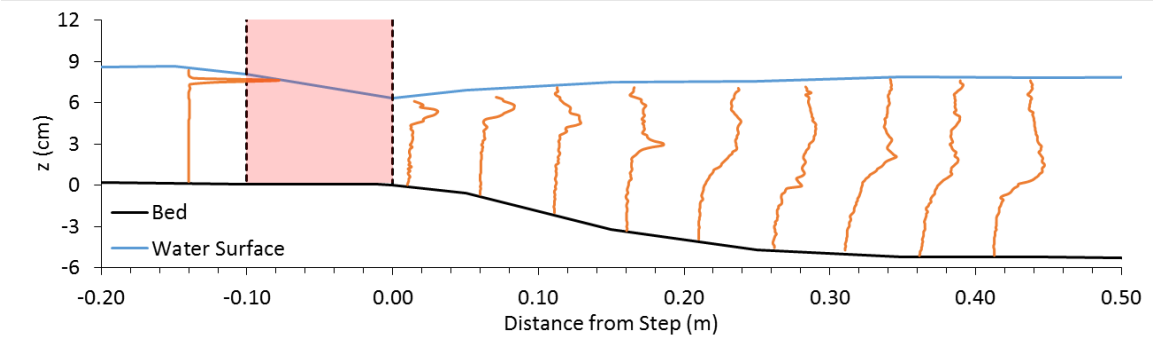

Figure G6. Fr_c = 0.92. Corresponding to Run C8. Dye concentration profiles using 35% constriction.

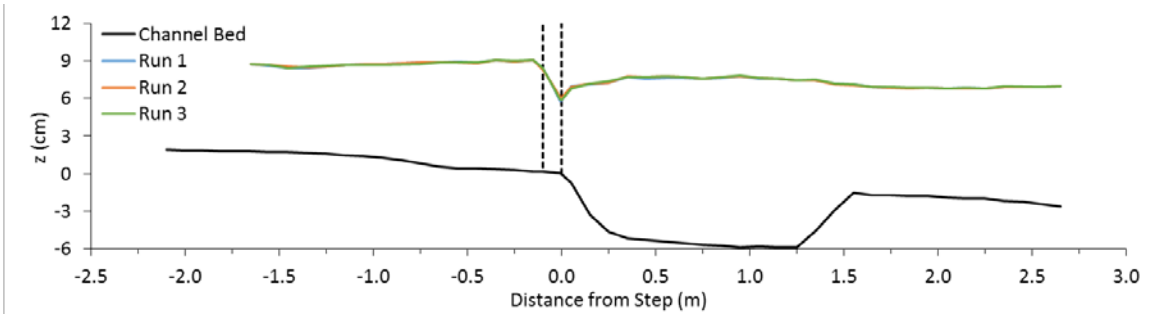

Figure G7. Fr_c = 1.01. Corresponding to Run C9. Water surface using 40% constriction. Location of constriction represented by dashed lines.

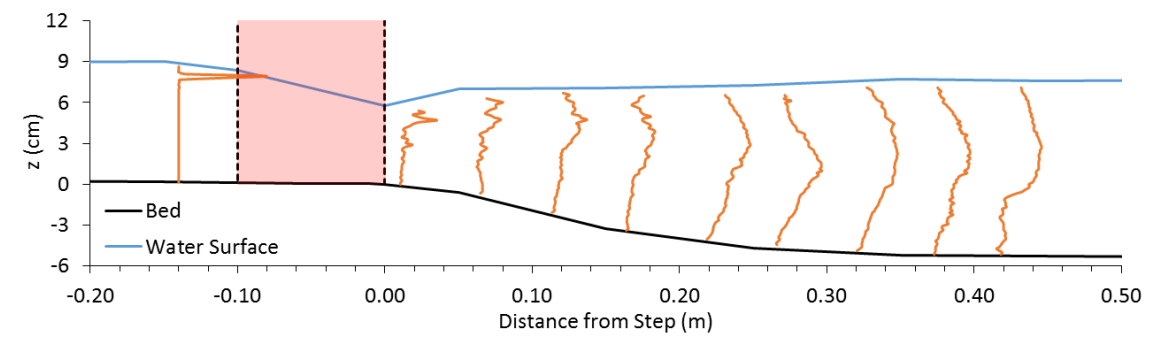

Figure G8. Fr_c = 1.01. Corresponding to Run C9. Dye concentration profiles using 40% constriction.

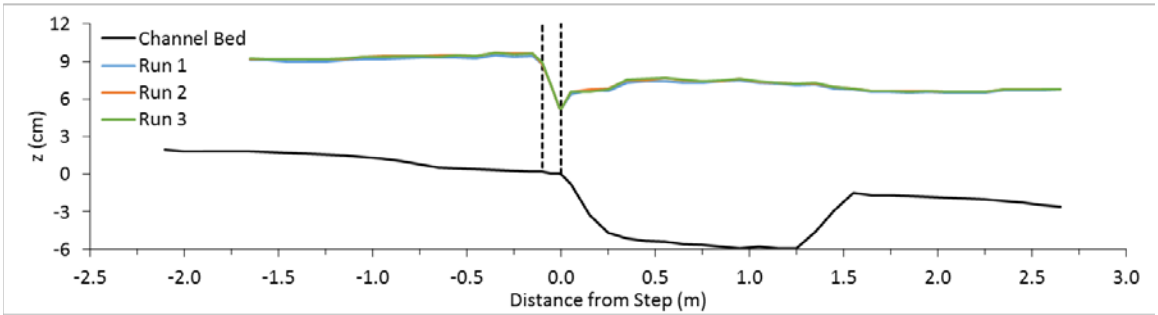

Figure G9. Fr_c =1.10. Corresponding to Run C10. Water surface using 50% constriction. Location of constriction represented by dashed lines.

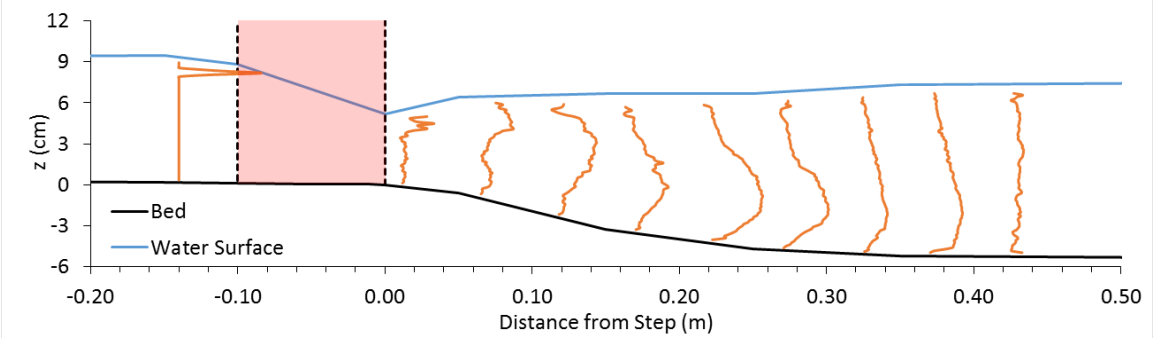

Figure G10. Fr_c =1.10. Corresponding to Run C10. Dye concentration profiles using 50% constriction.